Simultaneous shot separation

Typically, in seismic acquisition an active source is shot, and then a set waiting time must elapse before the next source point is acquired. This is to allow the energy to sufficiently dissipate, such that adjacent sources do not actively interfere. In simultaneous shooting, this restriction is relaxed (**?**; **?**; **?**). Despite this unvaoidable high energy overlap, many methods exist, or have been postulated, that can use these data very effectively. There are ways to design these surveys to minimise types of interference (**?**), to maximise acquisition potential (**?**), or to simply ignore the fact other sources are present (**?**).

The concept of recording overlapping data has many terms in modern nomenclature, often meaning subtly different things. Allowing active sources to overlap may be called blending, simultaneous shooting, or continuous recording, amongst others.

Chapter 3 discussed phase-encoding in detail. Of course, there are stark similarities between simultaneous acquisition and phase-encoding. From hereon, the former will be referred to as 'primary' blending, and the latter as 'secondary' blending. This language is intuitive, since during phase-encoding the data provided were acquired conventionally, making the blending a secondary process.

For phase-encoding, how to blend and combine these data was a key consideration. For field blended data, post-acquisition, the blending is fixed. There are encoding options available during acquisition - randomness of delays, waiting times, amplitudes, relative frequency contents etc, but once the user is given these data the blending can not be changed. This poses a variety of new problems for how to eventually image these simultaneously shot data, and how to optimally design a blended survey. This chapter will focus on designing a robust method for separating simultaneously shot data, under a variety of shooting patterns.

Initially, assuming the desired, final output is a clean, high-fidelity image, comparable to the image obtained from an unblended survey, then there are two clear options. One can attempt to directly image these data, or attempt to separate these overlapping data to approximate a conventionally acquired data-set, and image subsequently. The following sections will discuss the benefits and pitfalls from these two approaches.

IMAGING BLENDED DATA

Firstly, direct imaging of a simultaneously acquired data-set will be explored. As discussed in Chapter 2, either Reverse Time Migration (RTM), or linearised inversion can be used, the former being the first adjoint procedure of the latter.

Passive imaging

Naive migration of these data, as if they were unblended, has been increasingly referred to as 'passive' imaging of blended data (not be confused with the imaging of passive data). It follows from some simple algebra (and intuition) that the image will be plagued with cross-talk artifacts.

$$\sum_{i=1}^{n} \mathbf{L}_i \mathbf{m} \;=\; \mathbf{d} \tag{1}$$

If an operator, $\mathbf{L}$, describes all these data, as $\mathbf{Lm} = \mathbf{d}$, then $\mathbf{L}$ can be decomposed into individual shots, as shown in equation 1. Here, $\mathbf{m}$ describes the scattering potential field, $\mathbf{d}$ describes the entire data-set, and $\mathbf{L}_1$ relates the first shot, $\mathbf{d}_1$ to $\mathbf{m}$ etc., up to shot n.

Now, consider the case where $\mathbf{d}_1$ and $\mathbf{d}_2$ overlap, such that $\widetilde{\mathbf{d}} = \mathbf{d}_1 + \mathbf{d}_2$. Conventional migration applies $\mathbf{L}'$ to these data, where $\mathbf{L}' = \mathbf{L}'_1 + \mathbf{L}'_2$, and sums the result to form an estimate of $\mathbf{m}$. The result of this operation is formulated in equation 5.

$$\begin{aligned}
\mathbf{m} &\approx \mathbf{L}'\widetilde{\mathbf{d}} && (2)\\
&\approx \mathbf{L}'_1\widetilde{\mathbf{d}} + \mathbf{L}'_2\widetilde{\mathbf{d}} && (3)\\
&\approx \mathbf{L}'_1\mathbf{d}_1 + (\mathbf{L}'_1\mathbf{d}_2 + \mathbf{L}'_2\mathbf{d}_1 +)\mathbf{L}'_2\mathbf{d}_2 && (4)\\
&\approx \mathbf{m}_0 + \widetilde{\mathbf{m}}_0 && (5)
\end{aligned}$$

The imaging artifacts come from the operator that images $\mathbf{d}_1$ being applied to $\mathbf{d}_2$, and vice-versa. It is clear why this interference is known as crosstalk, since it comes from these cross-terms.

There are circumstances under which direct migration of these data results in an acceptable image. If shots are well separated by distance (Distance Separated Simultaneous Source, or DS^3, **?**), then this operator overlap is small, and crosstalk artifacts migrate outside of the domain of interest (or at least far from the imaging target). Furthermore, if the blending power is low (a relative measure of interference quantity), and the shooting dense, then the power of the stack will often mitigate these crosstalk artifacts. Since, whilst they are high amplitude on a shot-by-shot basis, they are incoherent between shots. The image may be unreliable for amplitude analysis, but for structural information, or for an initial model during inversion, it will be adequate. This is contingent on random time delays between sources, constant delays may not result in these artifacts stacking out as efficiently.

Whilst these two situations may result in adequate structural images, two problems remain. A better solution is needed for trustworthy amplitudes, and there is

an implicit background velocity model assumption. For direct imaging, especially linearised inversion, a representative velocity model is needed. This point will be elaborated upon during the rest of this chapter.

Imaging through inversion

Passive imaging of blended data can be improved by simultaneous inversion. Options include direct inversion for the scattering model (**?**; **?**), target oriented simultaneous inversion (**?**), inversion for separate time-lapse vintages (**?**), amongst others. Conceptually, this is similar to phase encoding, where the encoding is fixed, and α is a vector filled with ones.

From the discussion in Chapter 3, one can conjecture that convergence for this encoding sequence would be slow. Meaningful results can be recovered, however, by virtue of the fact the model space is still vastly smaller than the data space.

However, there is a more fundamental limitation with inverting blended data directly than slow convergence. Such a methodology would require accurate velocity control, which is crucial for linearised inversion and it's subclasses. If the velocity is not well constrained then the inverted scattering potential will be imaged incorrectly, and information will be lost. As an acquisition solution a stringent velocity requirement is unacceptable. Consequently, using direct inversion to image blended data is an interesting academic problem, but ultimately other solutions must be sought. This leads to the problem of simultaneous data separation.

SEPARATING BLENDED DATA

The most flexible, and velocity independent, option for processing overlapping data is to separate shots to individual records. Once this has been achieved a conventional processing flow can be followed. A methodology that is not strongly dependent on velocity or Earth model knowledge is desirable, since for exploration surveying a strong control on subsurface geology is an unreasonable expectation.

For shot separation, several approaches are possible. The concept of image space inversion will be the focus of this thesis discussion; other, existing, options will be briefly discussed and contrasted first.

Data space filtering

A cursory glance at simultaneous shot records may give an observer the notion that simple data space filtering could be used. For relatively flat geology, and with well distance-separated simultaneous sources, this is often the case. Successful data space filtering methods rely on either conflicting dips, or using the apex of events to ascertain

the shot of origin. However, once sources are proximate in both time and space, correctly identifying the origin of certain events in a shot record becomes difficult, and the dips of events can become more aligned. If the human eye is not able to distinguish these events, assuming there is limited prior model knowledge, then an algorithm will similarly fail. This is exacerbated for certain geologies, for example steeply dipping salt bodies. Reflections from these will appear at large offsets and late times, potentially causing them to become confused with other sources.

As an example, a group of randomly delayed shots are shown in Figure 1. In this figure it is largely possible to distinguish which shots are related with which reflection events. This can be contrasted with Figure 2, which shows two shots simulated over the same model, adjacent to a steep salt body.

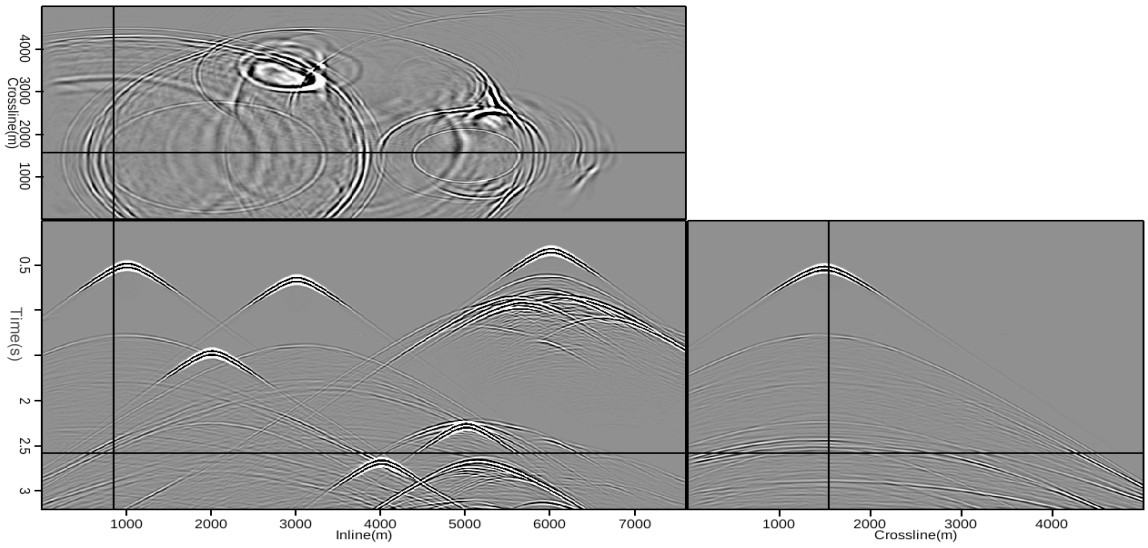

Figure 1: Five randomly delayed shots, while the record is noisy it is possible to distinguish which shot caused which event. [**CR**]

The concept of separating well distance-separated shots is almost moot. Filtering antithetic events is trivial, and often simply migrating these data as if there was no overlap provides reasonable result.

The majority of existing and effective techniques rely on using a domain transform, or series of transforms, which can isolate coherent parts of the signal. These all originate from the concept of randomised source intervals and receiver gathers (**?**). The pinciple of seismic reciprocity concludes that, for a given shot record, the same data would be recorded if all sources and receivers were swapped. In the situation where overlapping shot points are randomized, in time and space, then transforming to the common receiver domain will scramble much of the overlapping energy, resulting in what could be considered as a shot gather plagued with random noise. A variety of random noise reduction technqiues can now be invoked.

This can be further illustrated by looking at 2D gathers, for example in Figure 3 and Figure 4. Here the right hand panel is a corollary to the receiver domain, the left

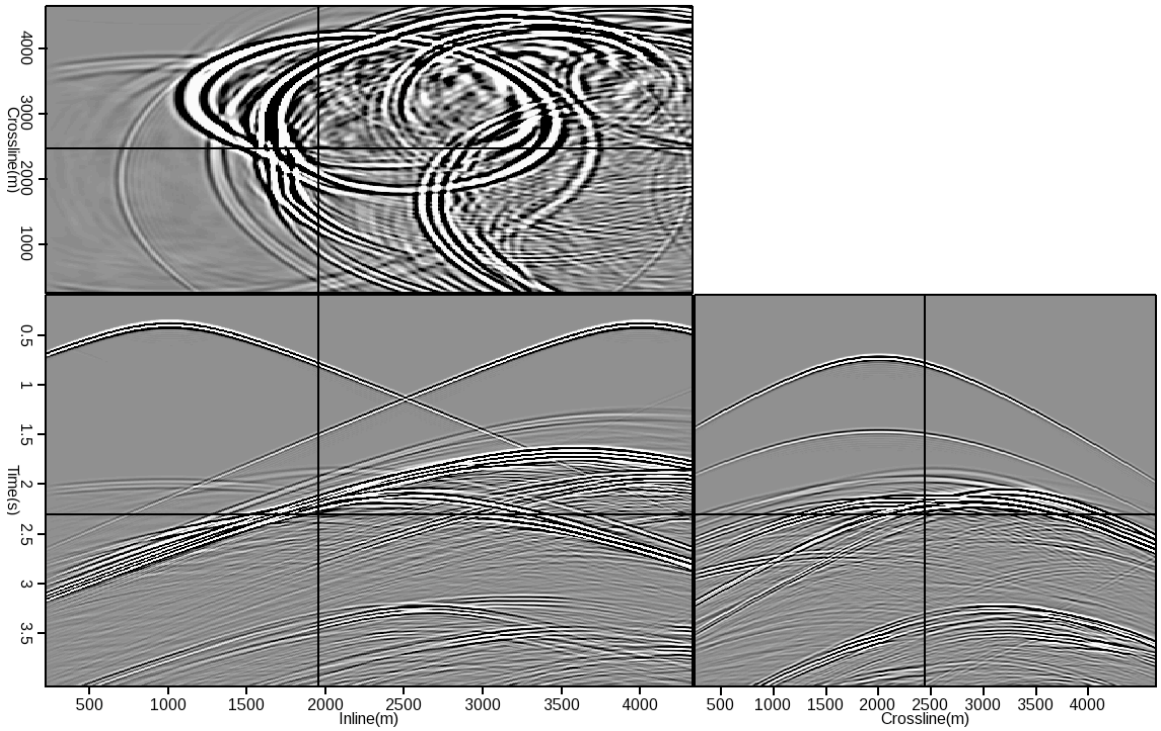

Figure 2: Two shots, simulated over the same model as Figure 1. At late times, it becomes impossible to ascertain which shots given events originated from. [**CR**]

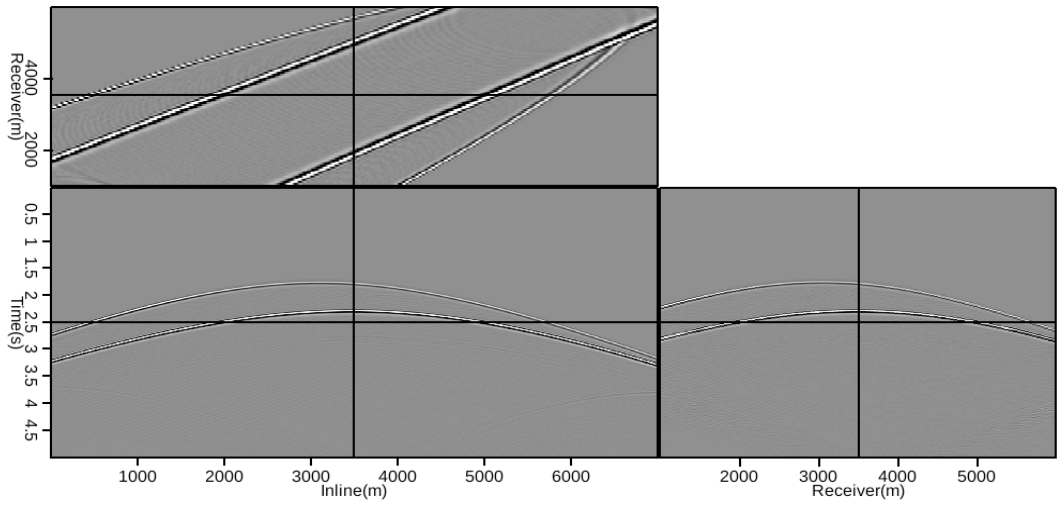

Figure 3: A simple dataset, from a two layer model. The left side panel is a shot gather example, the right side panel is a receiver gather. [**CR**]

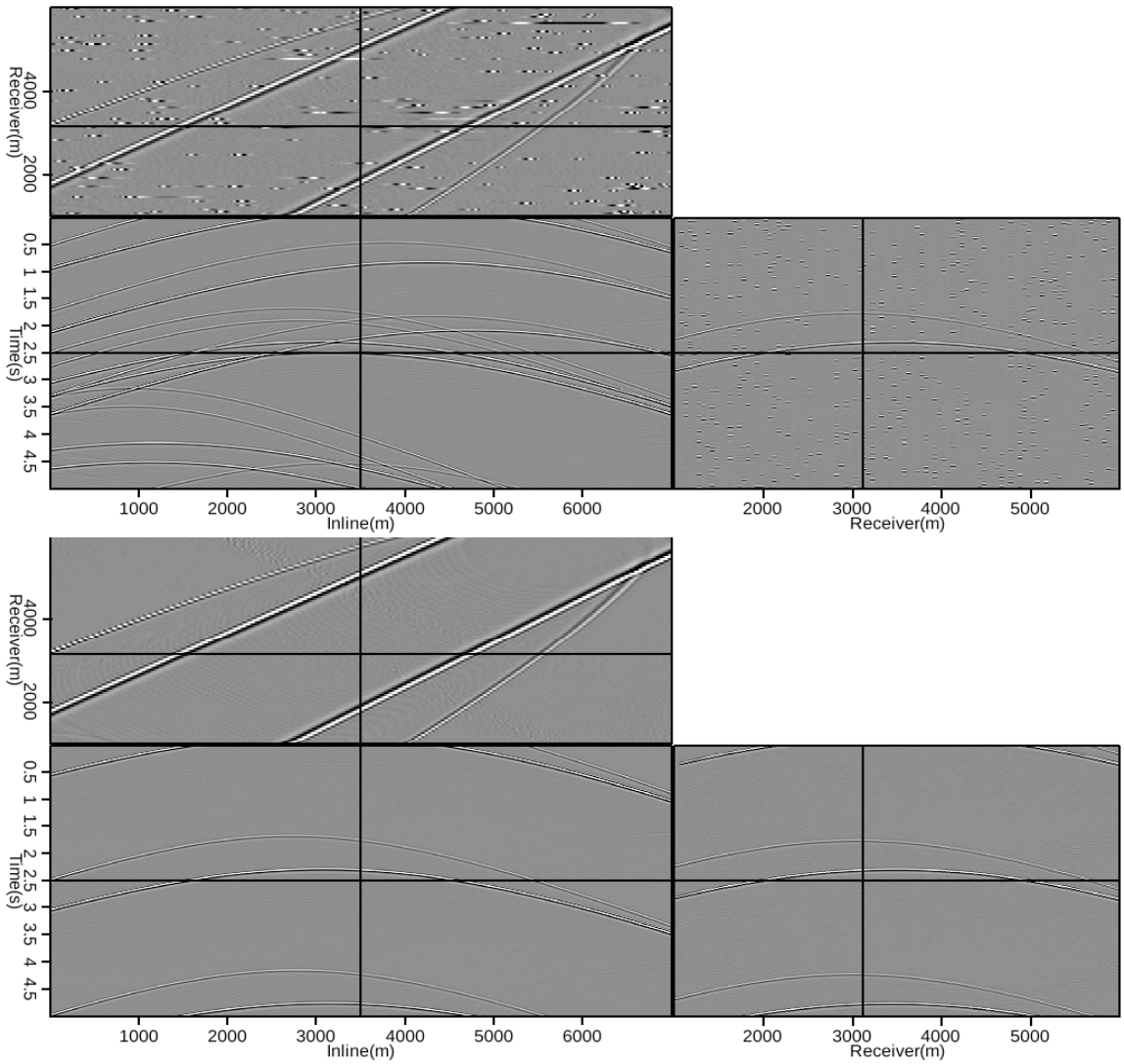

Figure 4: The same dataset as in Figure 3, after random blending (top) and linear blending (bottom). [**CR**]

to the shot domain. The difference in coherency is extremely evident when comparing the top and bottom panels.

The bottom panel in Figure 4 highlights another potential pitfall, if the delays are constant then there are no coherency differences between these domains. As a result, any attempt to treat overlapping shots in the receiver domain as random noise will fail, and primary information will be lost.

Data space inversion

For randomised source timings, inverse methods based in the data space can be very effective in the field of simultaneous source separation; most of these use a variety of domain transformation, as mentioned above. **?** showed that using a Projection Onto Convex Sets (POCS) methodology, in the common receiver domain, results in a high degree of separation. Whilst effective, this technique involves many multi-dimensional Fourier transforms (**?**), so for certain geometries and blending schemes separation as a function of compute time may be slow.

Other receiver-gather projections can also be used. Both median filtering (**?**) and sparse radon transforms (**?**) are effective for many survey types and can be powerful tools for noise reduction. Additionally, threshholded interference reduction (**?**) and interference estimation (**?**) show promising results for data blended in 2D. Approaches borrowed from multiple prediction literature have been shown to have varying results, but often prediction-and-subtraction methods have yielded excellent separation (**?**).

? looked at a variety of advanced blending patterns and analysed how to invert for the transform that will link the source and receiver domains. Other successful methods use a compressive sensing approach (**?**), where many wavelet transforms can be used to separate these data.

All these existing methods strongly rely on random source delays, and any repetition or predictability in the source timings can induce surprisingly detrimental artifacts. **?** showed a number of interesting observations from field blending tests. Natural variation in the recharge time of these airguns can often provide a sufficient level of shot randomness. However, as survey size increases, so does the risk of underlying shooting predictability occurring in certain shot sequences. This is counter-intuitive in the field of seismic imaging, since generally an increase in survey size results in more redundancy and higher fidelity. It is possible to mitigate this potential repetition by inducing more unpredictability, such as by adding an extra time delay. This can be determined from a random number table, and induced once the airgun is recharged.

Theoretically, these inverse methods can handle many interfering shots. In practice, for marine acquisition, no more than three or four interfering sources are present at a given instant. This is a function of physical space, and availability of source boats. On land many vibroseis trucks have been used at once for a high degree of

parallel acquisition (**?**; **?**). It should also be noted that land acquisition provides a few other advantages for separation; different sweeps can be encoded to encourage orthogonalit and source positions are easier to randomise.

For these reasons, simultaneous land acquisition has been used extensively, and shown to give impressive results. There has been a marked increase in simultaneous marine acquisition, but some issues remain. For these reasons subsequent sections will be limited to the discussion of marine surveys, and will focus on a blending power of around three.

The image space

It is desirable to choose a domain, or inversion technique, which is less restrictive of blending pattern. In particular, developing a scheme which is robust while separating data acquired with constant or pseudo-constant delays is sought, since these aforementioned data-space methods fail under these conditions. By projecting the problem into the extended image space, these previous shortcomings can be circumvented. Although RTM is used as the transform operator, the use of an extended domain (either in offset or angle) loosens the restriction of having an accurate velocity model, which was alluded to in Chapter 2. No information is lost this way, and correct data reconstruction is achievable.

Furthermore, a technique that uses the image space can be easily augmented with a velocity update scheme - most of the necessary computation will already be done. This strengthens the potential of such an approach, as an improved velocity model will allow for cheaper, more accurate shot separation, during the next set of iterations. This will be elaborated upon subsequently.

Through image space projection, 'primary' shots of interest can be focused on (migrated, essentially), while overlapping energy, from 'secondary' shots, will be dispersed. This allows separation criteria to focus on both move-out differences and focusing contrasts. This is simply done by combing the input data into discrete shot records, according to a suggested recording time length and a set of shot timings. This results in a data-set which is the size of the would-be conventional data, but plagued with overlapping, coherent events.

Using the extended image space to remove coherent noise sources has been previously analysed, albeit under other objectives. **?** looked at using apex-shifted parabolic-Radon transforms to successfully remove surface related multiples. **?** looked at using F-K transforms from the extended image space to successfully remove imaging noise. However, in these cases the final imaging procedure had been completed, and this step was to remove some coherent artifacts before stacking to the zero-offset image.

The implicit goal herein is a separated dataset. As a result, transforming from the extended image space back to the data space is necessary - this is sometimes

termed demigration (**?**). Using demigration for multiple removal has been effective in several studies (**?**; **?**), and this is a similar problem to that of source separation. For amplitude consistent recovery, one pass of extended Born modeling (demigration) is insufficient, and inverse demigration is necessary (**?**). The process of demigration is equivalent to Born modeling, so for clarity the term inverse Born modeling will be used to describe linearized forward modeling as an inverse process, rather than inverse demigration.

Such inverse Born modeling methods have been shown to give full data recovery (**?**), and to remove multiples (**?**), although it has been an only lightly explored subject. To formally introduce this concept Born modeling must be revisited, and the extended image space will be introduced in full.

The extended image space and Born modeling

$$I(x,y,z) = \sum_{i}^{nshots} \sum_{t} P_s(x,y,z,t;\mathbf{s}_i) P_r(x,y,z,t;\mathbf{s}_i), \tag{6}$$

$$I(x,y,z,x_h,y_h) = \sum_{i}^{nshots} \sum_{t} P_s(x+x_h,y+y_h,z,t;\mathbf{s}_i) * P_r(x-x_h,y-y_h,z,t;\mathbf{s}_i). \tag{7}$$

If equation 6 describes Claerbout's zero-offset imaging condition, then an example of extended imaging can be described by equation 7. Here, $I(x,y,z)$ is the image in space, P_s is the source wavefield and P_r is the receiver wavefield; s_i represents the current shot of interest. If lag coordinates (known as subsurface offsets) in x and y are introduced (x_h and y_h), a 5D image can be created. It is possible to have lags in both t and z to create a 7D image, or any combination thereof.

If the correct velocity is used for extended migration, then an image sharply focused at zero-subsurface-offset is created. All the necessary kinematic and amplitude information for data reconstruction is contained in this zero-subsurface-offset image panel, an example can be seen in Figure 5. Artifacts present are a result of limited acquisition and data truncation, and will not hinder reconstruction. Next, Figure 6 shows the same data, but migrated using a constant velocity model (incorrect up to 20%). This zero-offset panel is now not sharply focused, and coherency over a range of subsurface offsets is observable. In this case much of the necessary kinematic and amplitude information, critical for accurate extended Born modeling, is spread over these offsets. Consequently, these must also be back-projected for accurate data recovery.

It is possible to apply an additional transform from subsurface offset to the angle domain. By measuring event curvature as a function of this opening angle, velocity

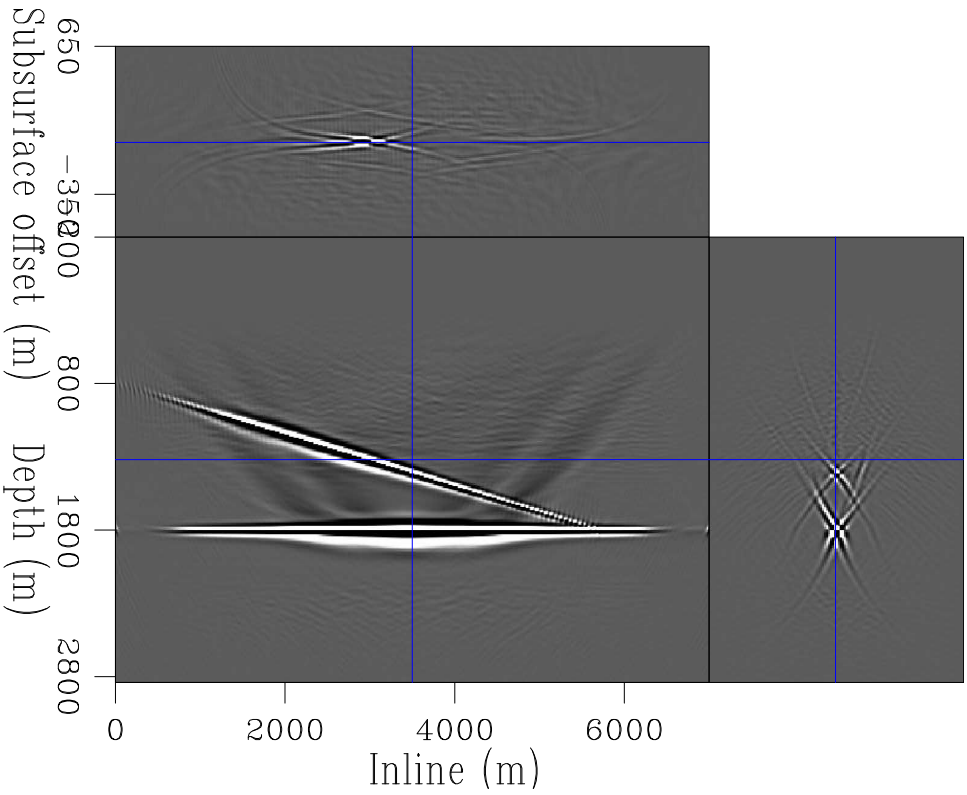

Figure 5: The unblended simple dataset, as seen in Figure 3, migrated into the extended domain with the correct velocity. [**CR**]

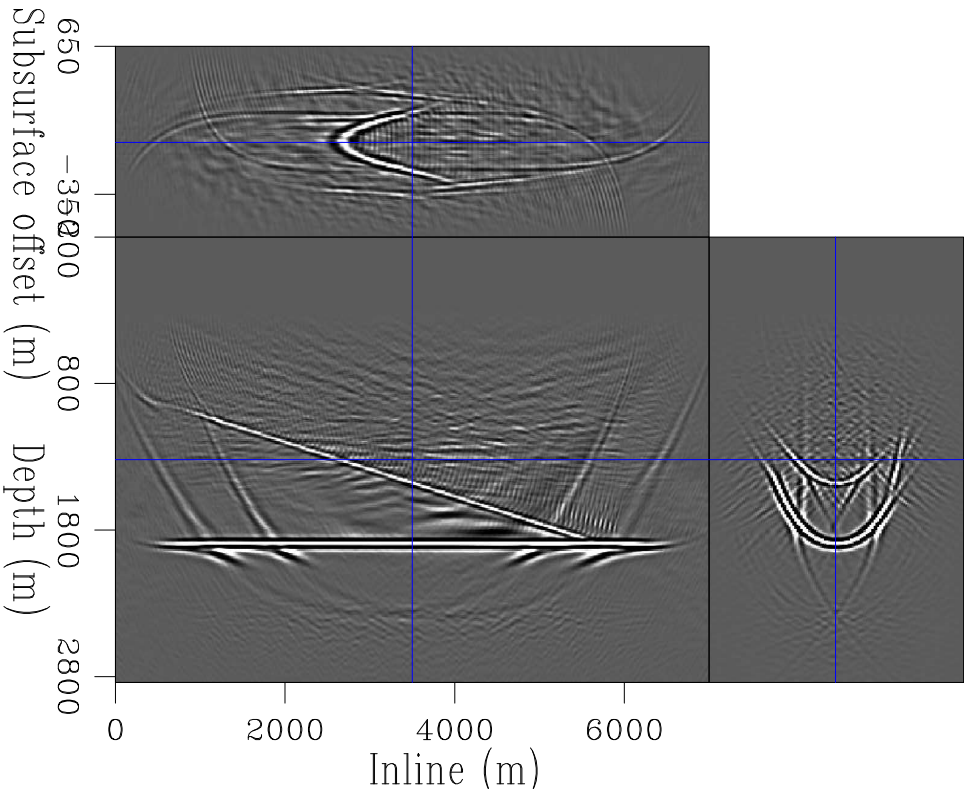

Figure 6: The unblended simple dataset, as seen in Figure 3, migrated into the extended domain with using a constant velocity model. [**CR**]

model updates can be estimated. It is by this approach that Wave-Equation Migration Velocity Analysis (WEMVA) works (**?**). For many algorithms the angle domain is used instead of the subsurface offset domain, since this parameterisation is directly relatable to surface geometry and velocity. The concept of suburface offset itself is somewhat unphysical, but during extended imaging it provides the necessary degrees of freedom to preserve input wavefield information.

In addition to this simple, two-layer dataset, two more complex and geologically representative models will be used. These are a slightly modified version of the reference Marmousi model (**?**) (padded with a water layer), and a windowed subsection of the latest SEAM model (**?**). Initially, the Marmousi model will be used to investigate if this added complexity poses additional difficulty for inverse Born modeling, and how these results vary under different blending experiments. The velocity models used, and the reference unblended dataset, are shown in Figure 7 and Figure 8. For this dataset, 60 shots were simulated with a spacing of 100 m, receivers were all along the top of the model.

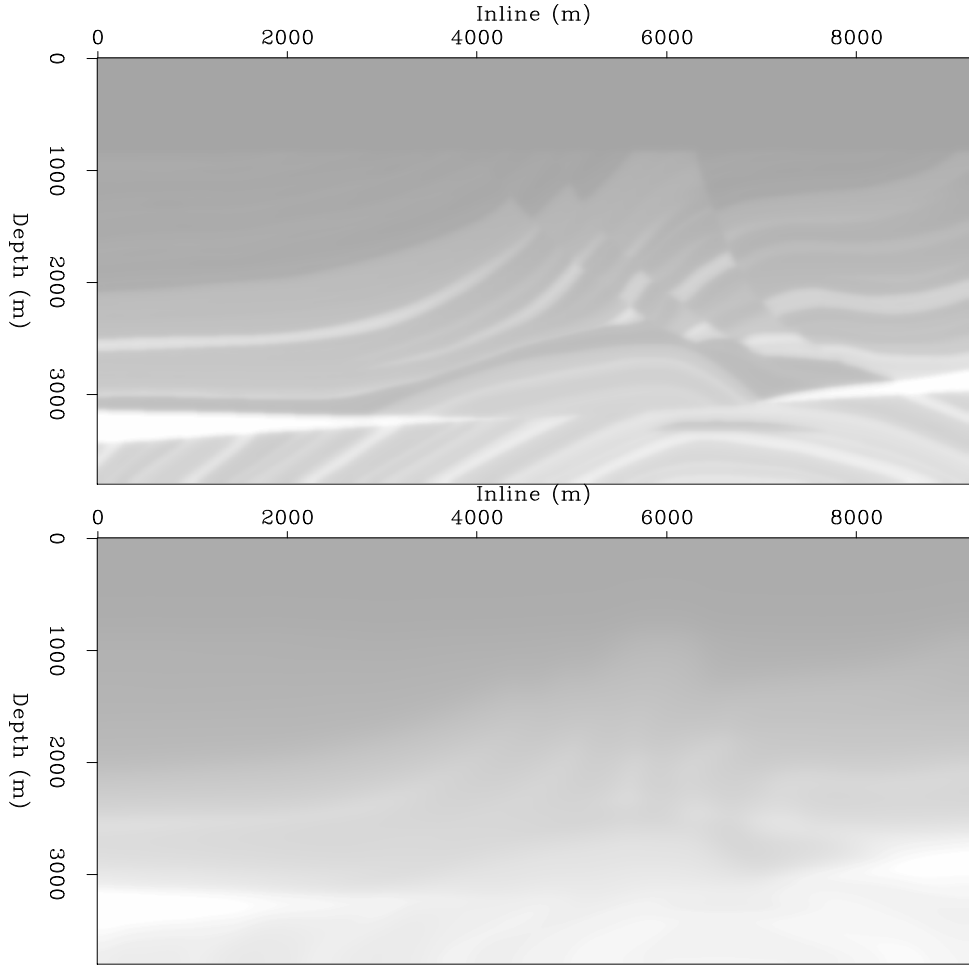

Figure 7: Accurate and smoothed representations of the Marmousi velocity model. [**ER**]

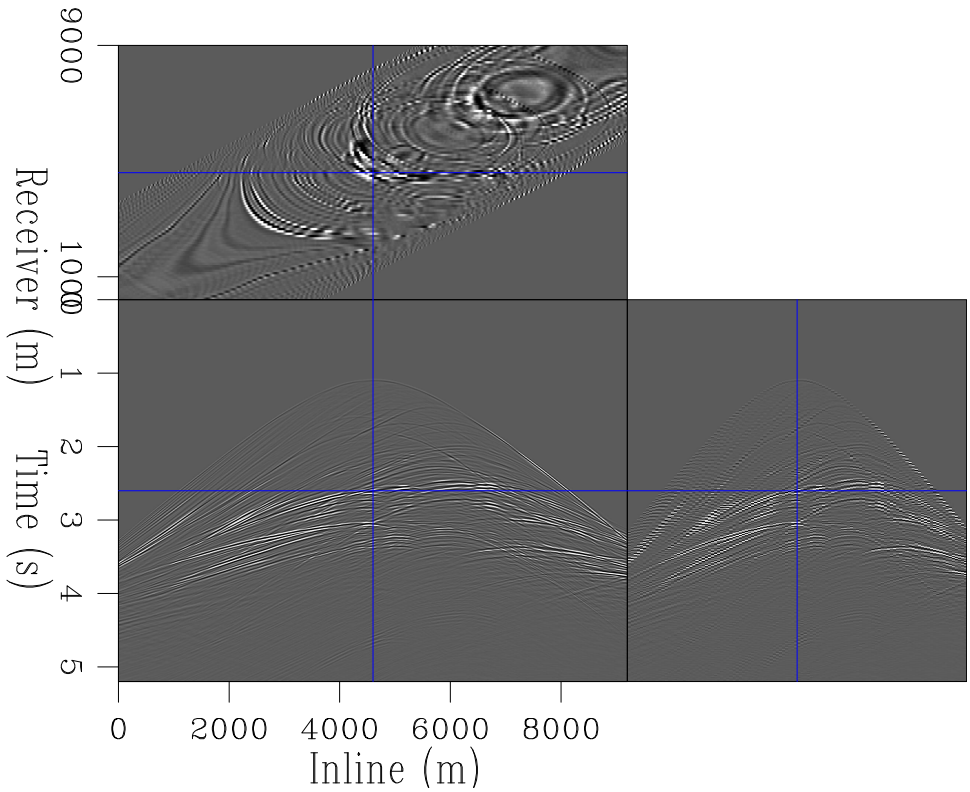

Figure 8: Data acquired over the Marmousi model. [**CR**]

Random delays

Random delays between source times and positions provides the most options for data separation. Figure 2 already showed the simple two-layer dataset, with both random and constant delays simulated. The implications of these scenarios will now we analysed in more detail.

The left-side panels (of Figure 2) show examples of shot gathers, there is a significant amount of highly coherent noise throughout these records. The right-side panel shows example receive gathers (since the recorders were fixed.) Noticeably, for random delays the overlapping noise takes on a highly different characteristic - the data of interest (primary events) are coherent, and all of the contamination has now been incoherently scrambled.

Inducing small delays between sources was an early style of simultaneous acquisition, known as dithering (**?**). Scrambling this noise was done through a simple, and very cheap, domain transformation, typically to an F-K space. The noise is spread over a large range of spatial and temporal frequencies, whilst the primary information is more tightly contained. This can be exploited in a number of ways - filtering, threshholding, inversion etc.

Figure 10 then show these randomly delayed data after imaging, migrated with

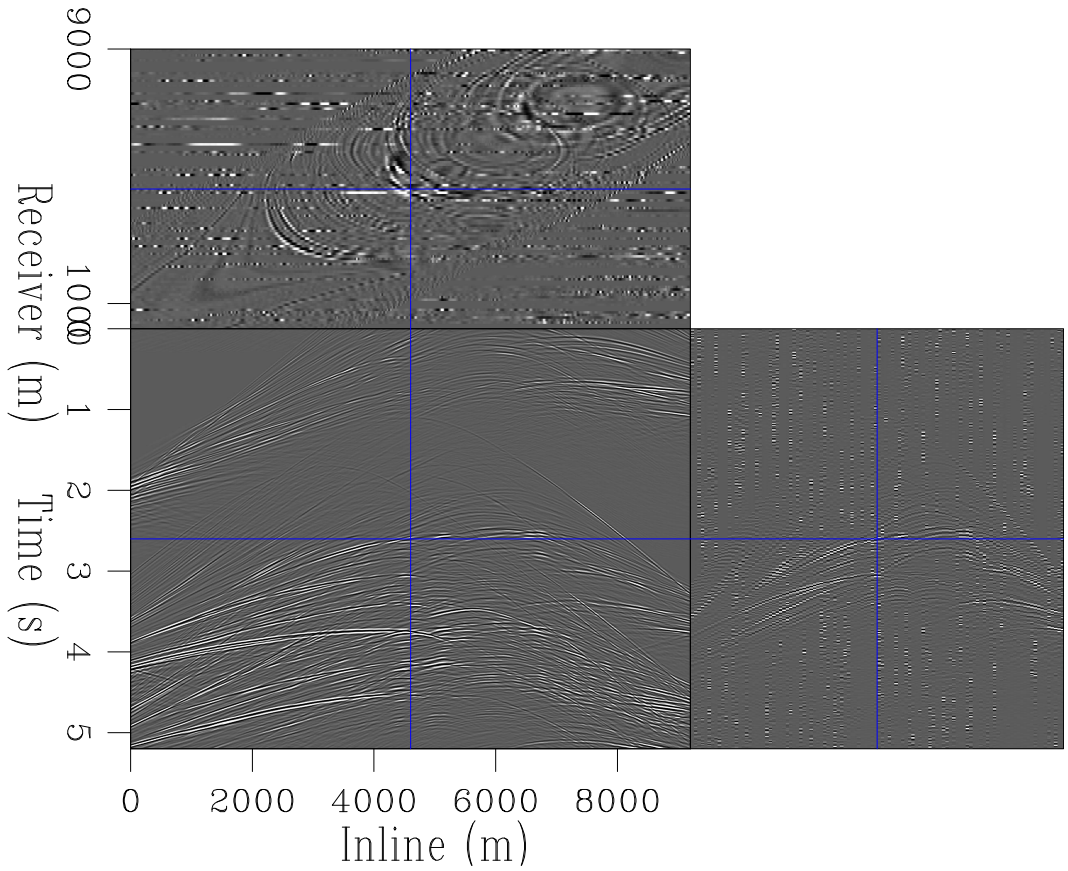

Figure 9: Data acquired over the Marmousi model using a random delay function. [**CR**]

the correct velocity model. The majority of this overlapping energy has stacked out, but there is a significant amount of high-wavenumber noise remaining in the image. This makes this simple imaging acceptable for structural / model building work flows, but will be insufficient if any amplitude work is desired.

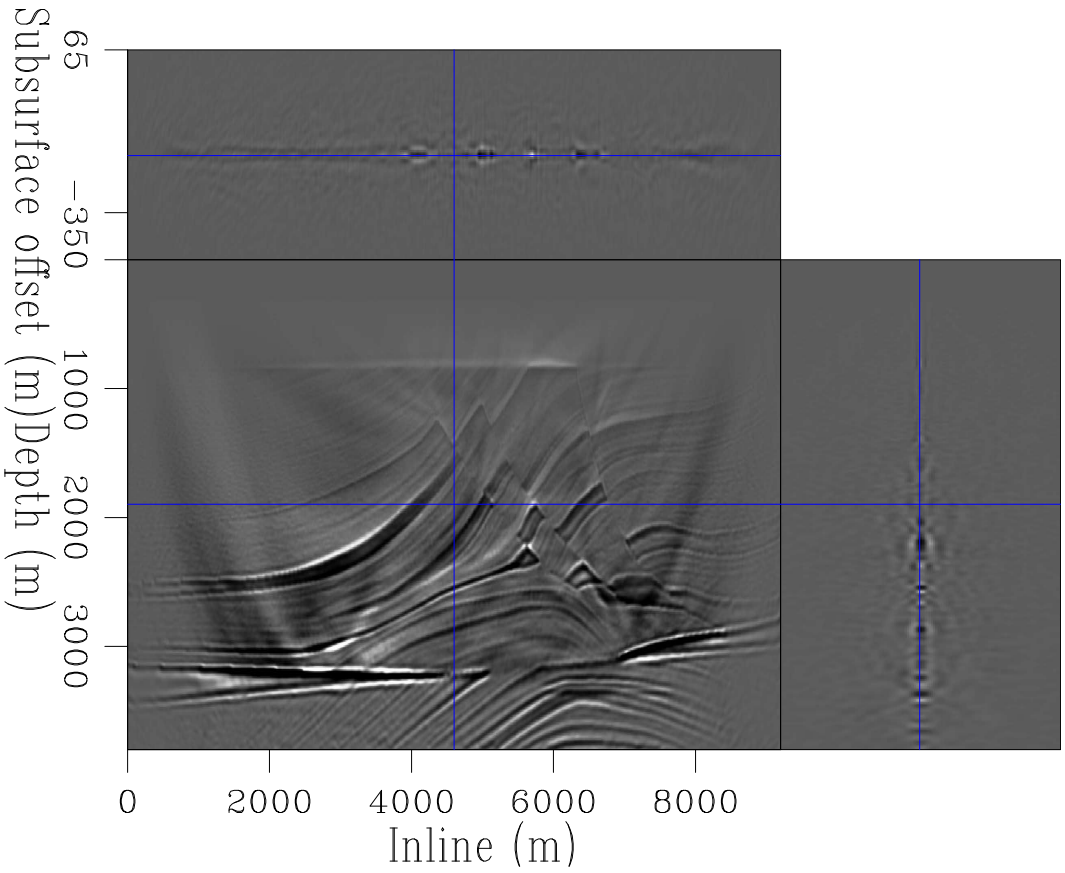

Figure 10: The extended image from migrating Figure 9 (data acquired using a random blending function) [**CR**]

Linear delays

A constant shift between source locations and timings will be denoted as 'linearly' delayed data, and this can pose some interesting, additional problems.

Figure 11 shows these Marmousi data, but this time the shooting pattern features a constant delay. Thus, there is no incoherency to exploit in the common receiver domain. This is further illustrated by looking in the F-K domain, the signal and the noise remain tangled, and techniques like filtering and threshholding will fail at removing the noise, and may remove primary information.

Imaging these data, with the correct velocity, gives the result in Figure 12. Somewhat surprisingly, the image is not plagued with high-amplitude artifacts. The reason

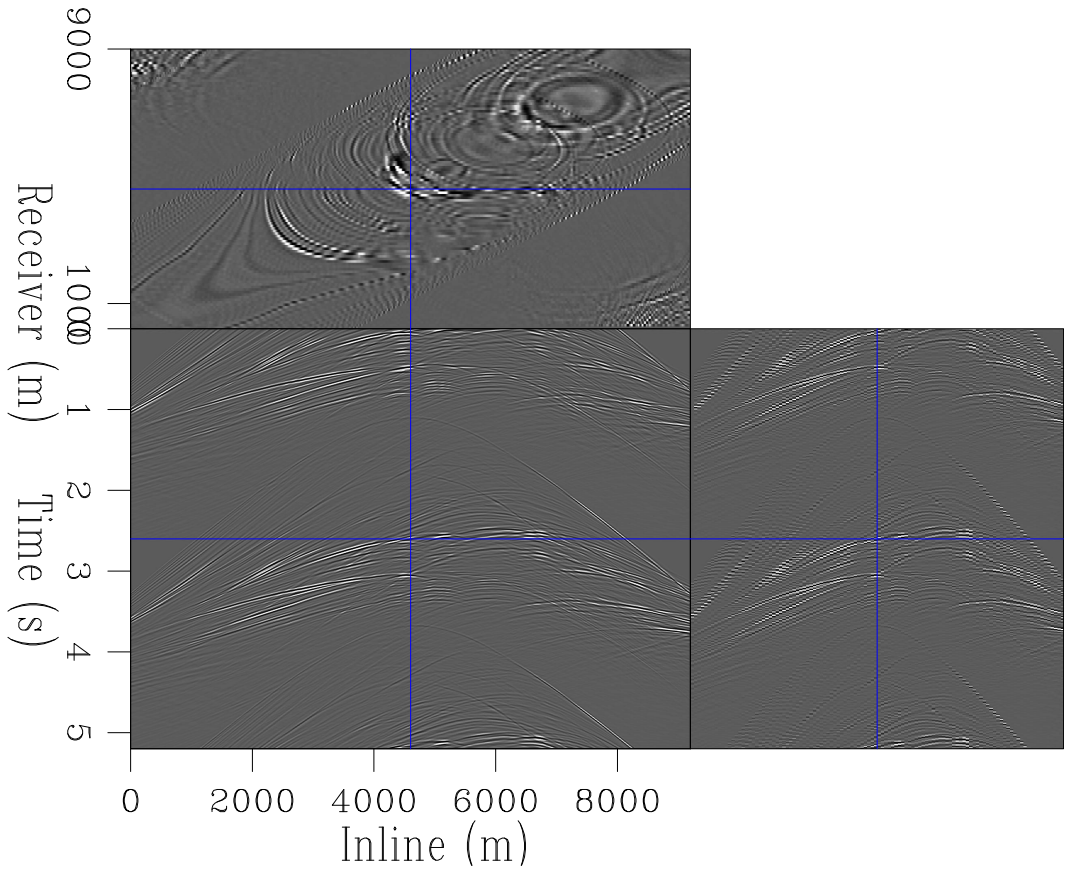

Figure 11: Data acquired over the Marmousi model using a linear delay function. [**CR**]

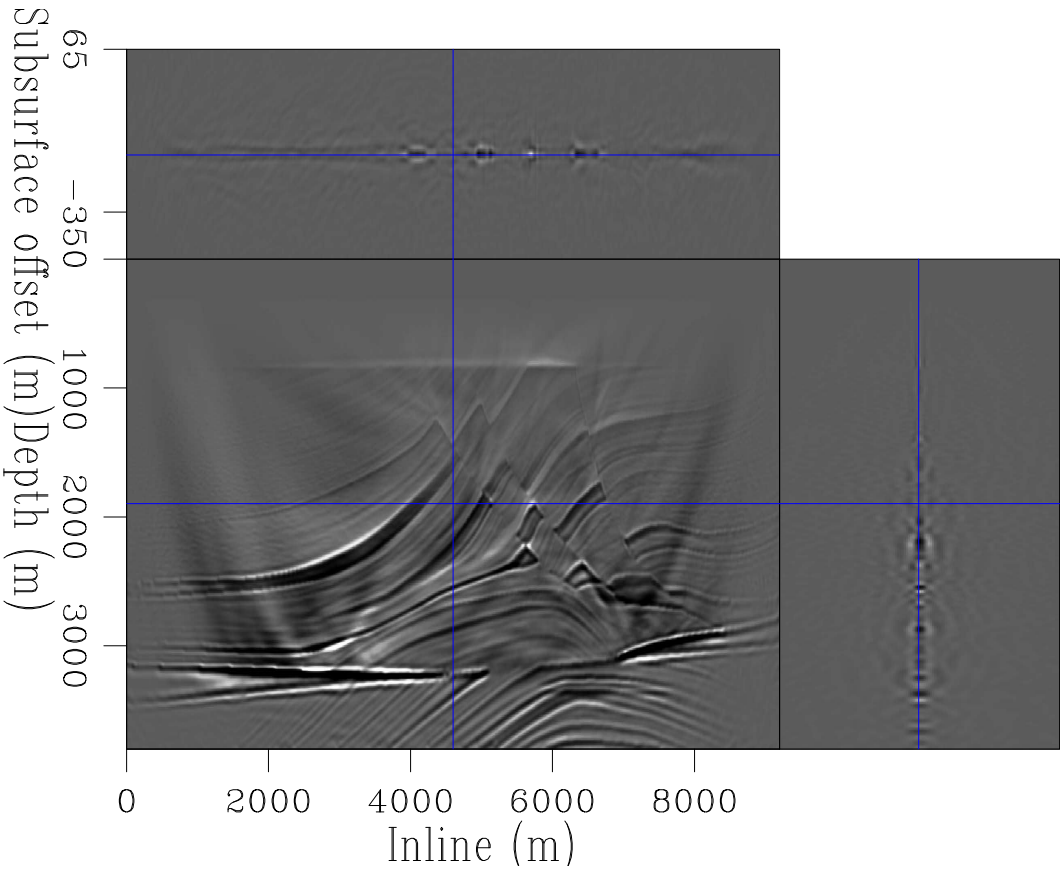

Figure 12: The extended image from migrating Figure 11. [**CR**]

for this is a little more subtle - because the blending style was not very aggressive, a lot of the noise either does not correlated into the image, or migrates outside of the domain of interest. These is still some noise, relative to the conventional image, but this is less damaging than in the random case. Additionally, these artifacts are comparably high-amplitude if single-shot images are observed, however these artifacts are still incoherent between images. Thus, stacking removes much of the noise which was migrated into the target area.

Pseudo-linear delays

The most realistic marine acquisition scenario is often that of pseudo-linear delays. These are close to constant shifts, but with a jitter of around 5% between times.

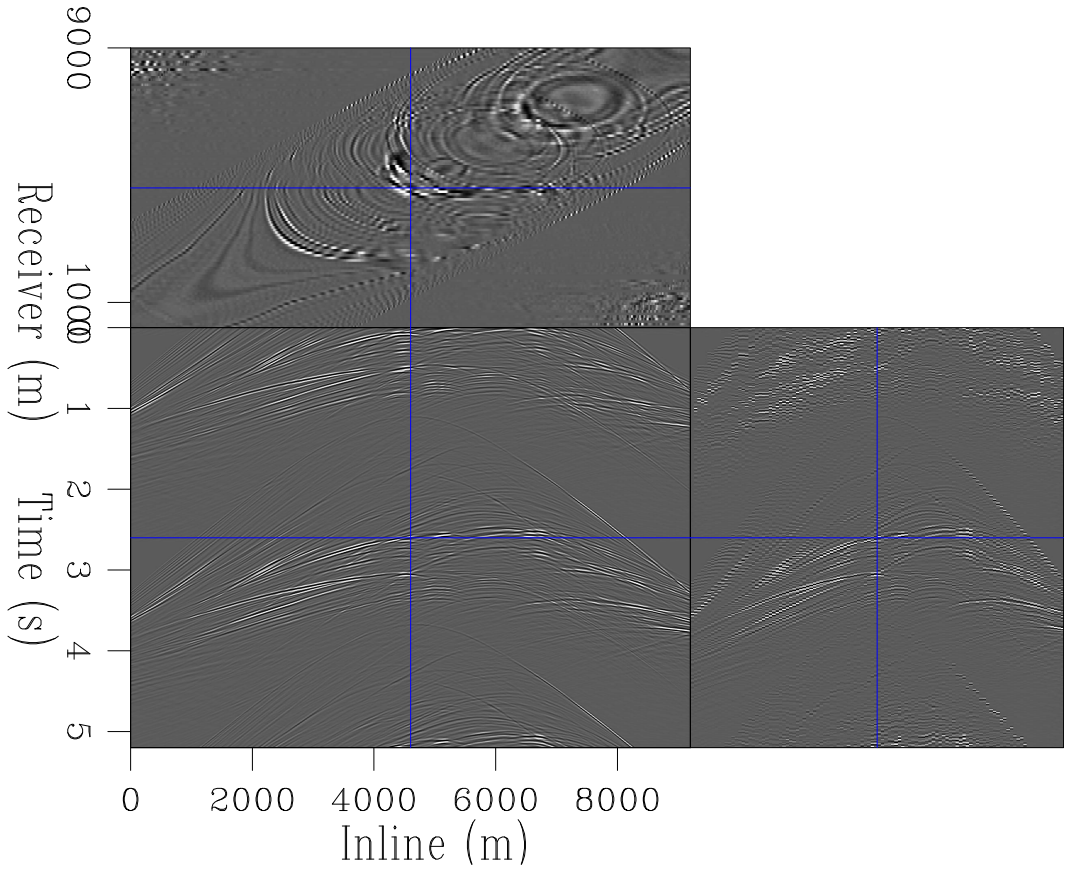

Figure 13: Data acquired over the Marmousi model using a pseudo-linear delay function. [**CR**]

This small amount of randomness creates a high level of incoherency between domains; migrating these data gives similar results to the linear delays, and again, these are cleaner than for random delays. Largely, this is due to the temporal separation of the signal and noise. The slight randomness then provides the additional incoherency needed to largely stack out the noise.

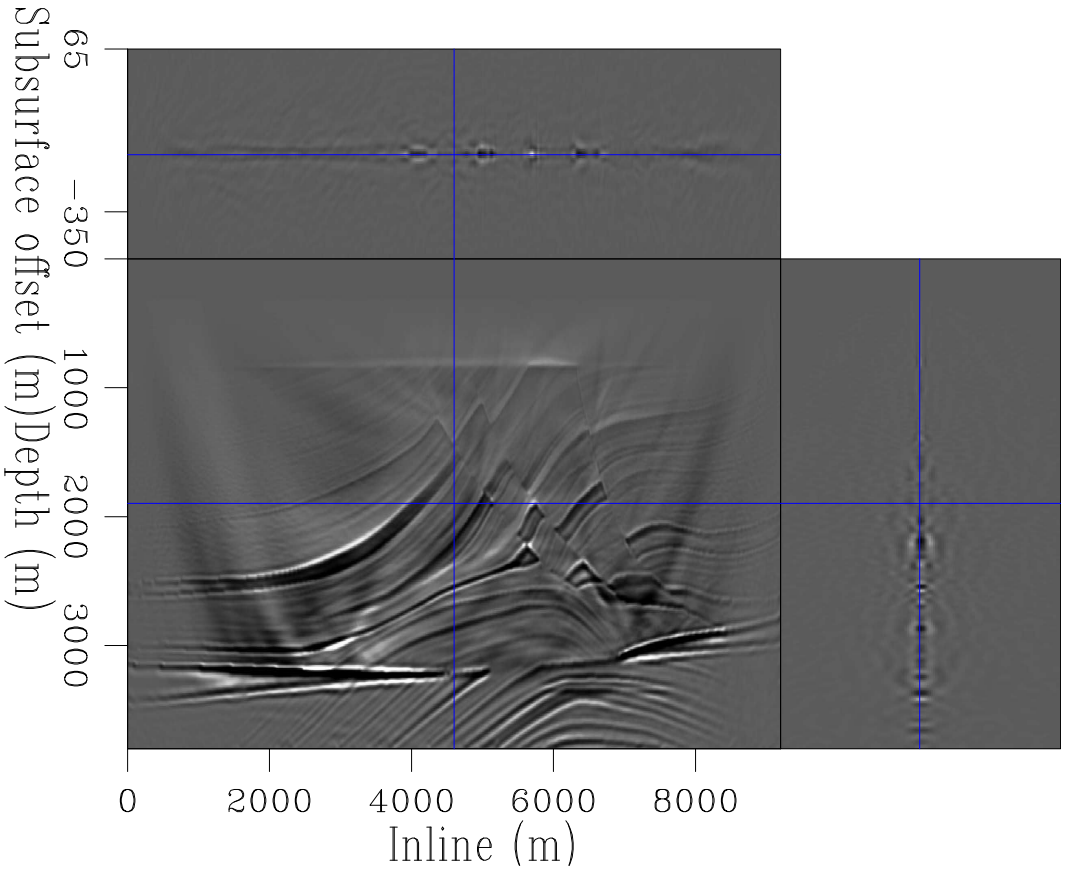

Figure 14: The extended image from migrating Figure 13 (data acquired using pseudo-linear delays). [**CR**]

Angle domain inversion

From studying the two-layer model subsurface offset panels, particularly under linear blending conditions, it appears that blended energy could be isolated as a function of curvature, and hence removed. If it is possible to remove contaminated energy from these panels, then the images could be demigrated, and data separation achieved. To test this theory, this two-layer dataset, with linear blending, will be used. Figure 15 shows the correct velocity image, and an image constructed from a velocity which was scaled to be too slow. In both of the subsurface offset panels, events from the data of interest ('primary' events) and events from the blended energy ('secondary' energy) are both easily identifiable. However, for the incorrect model the events now all have significant curvature, and the focusing contrasts are less pronounced.

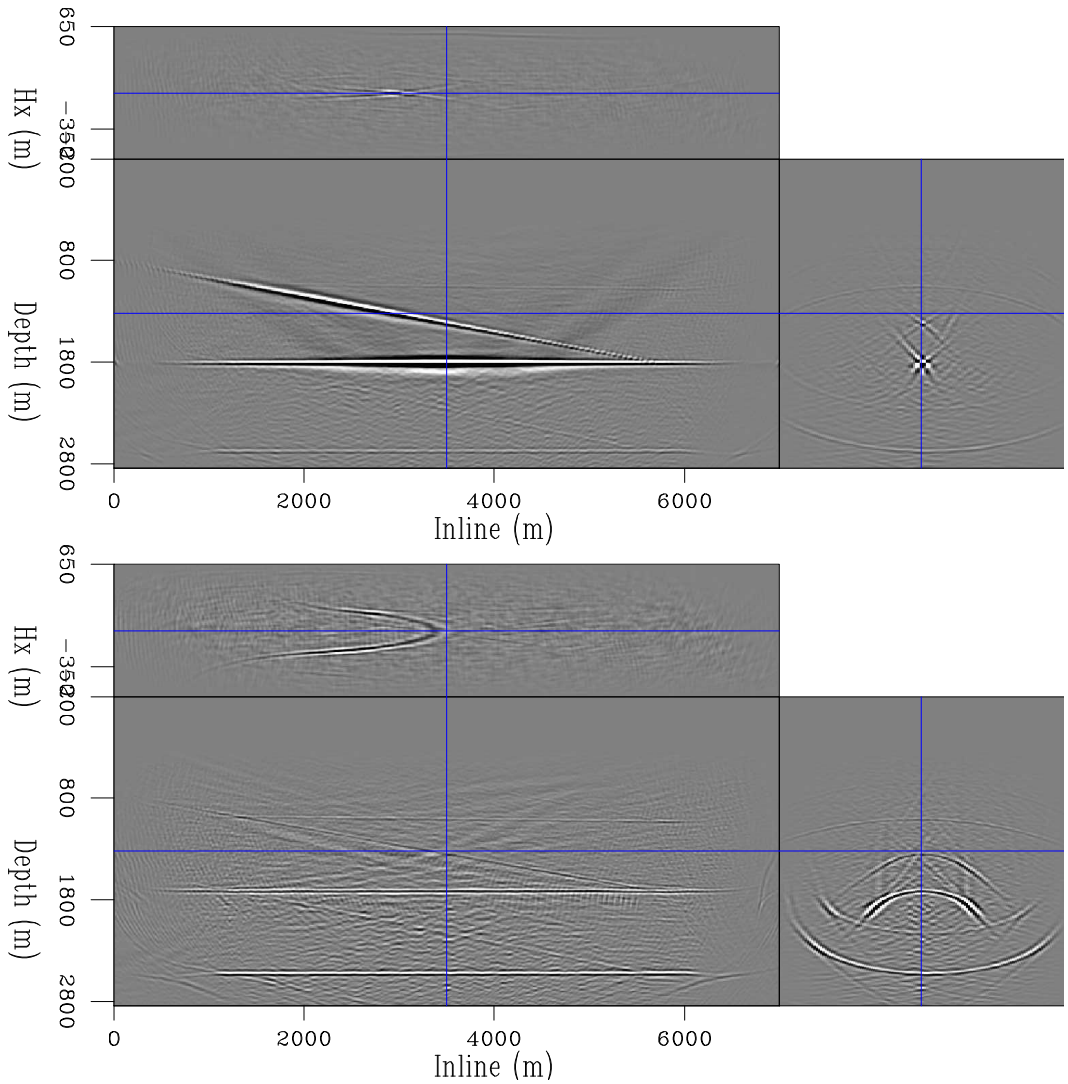

Figure 15: Linearly blended data migrated into the subsurface offset domain using the correct velocity model (top) and a model 10% too slow (bottom.) [**CR**]

A second domain transform is necessary, such that events can be isolated as a function of curvature. A parabolic Radon transfrom was selected, since for a flat reflector the curvature of these events should approximate to a parabola. However, applying a parabolic Radon transform to the top panel will be problematic, since some events have been focused to a point - this will cause this information to become spread out in the Radon domain. Instead, another transfrom must be used before moving to the Radon domain, and this is a transform to the angle domain. Measuring the curvature of these events in the angle domain is how WEMVA updates are constructed.

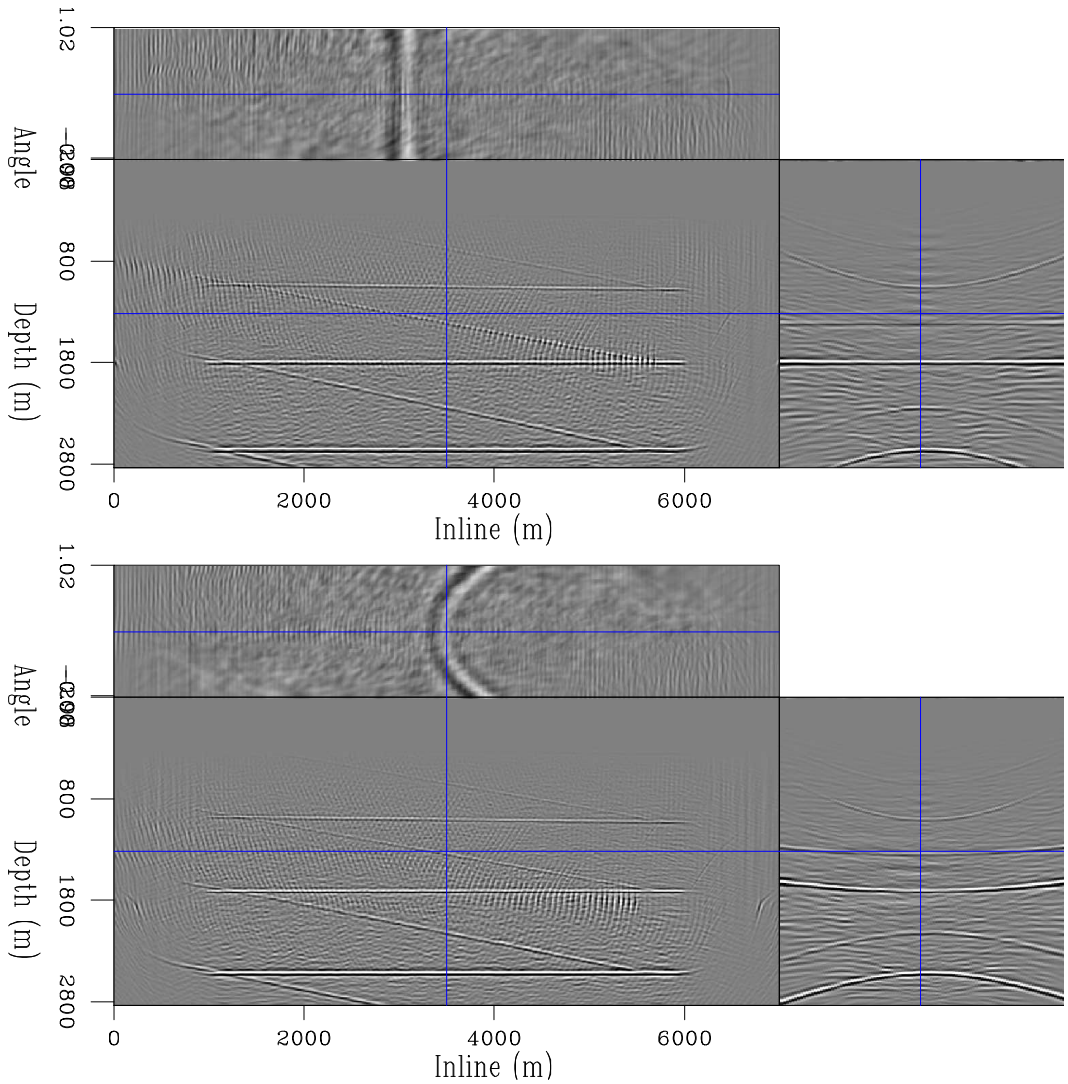

Figure 16: The same images as Figure 15 but with the third axis transformed into the subsurface angle domain, rather than subsurface offset. [**CR**]

The angle domain representation is shown in Figure 16. The previously well-focused events now appear flat, and the curvature of other events have become more extreme. It is now possible to transfrom to the parabolic Radon domain, and isolate

events by this curvature.

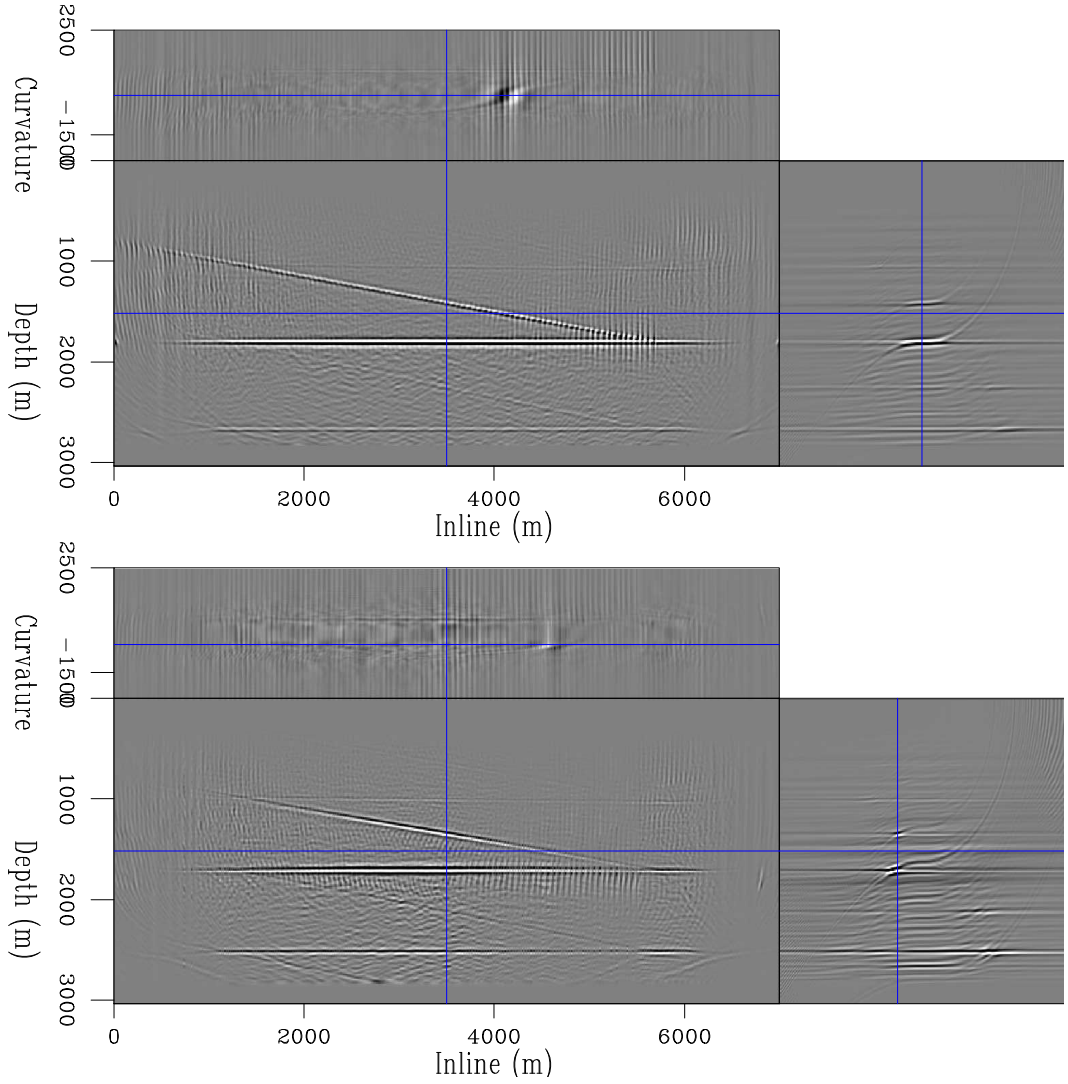

Figure 17: The angle domain image with the correct velocity model after a single parabolic transform (top) and the slow velocity image after a single parabolic radon transform. [**CR**]

However, a parabola is not an ideal representation of these events, and nor is the Radon transform used very exact (due to aperture restrictions). These limitations are manifested in Figure 17; whilst some curvature separation has been achieved, events have not been well focused as function of their curvature, and there is a lot of contamination across this space. It is possible to extend this domain transformation to an inverse process, and the result is shown in Figure 18. After ten iterations of this process, coherent events are now well focused at a given measure of curvature. It would be possible to window these events and reverse these processes, resulting in a separated dataset.

This process has two key problems implicit in these assumptions. One, is that

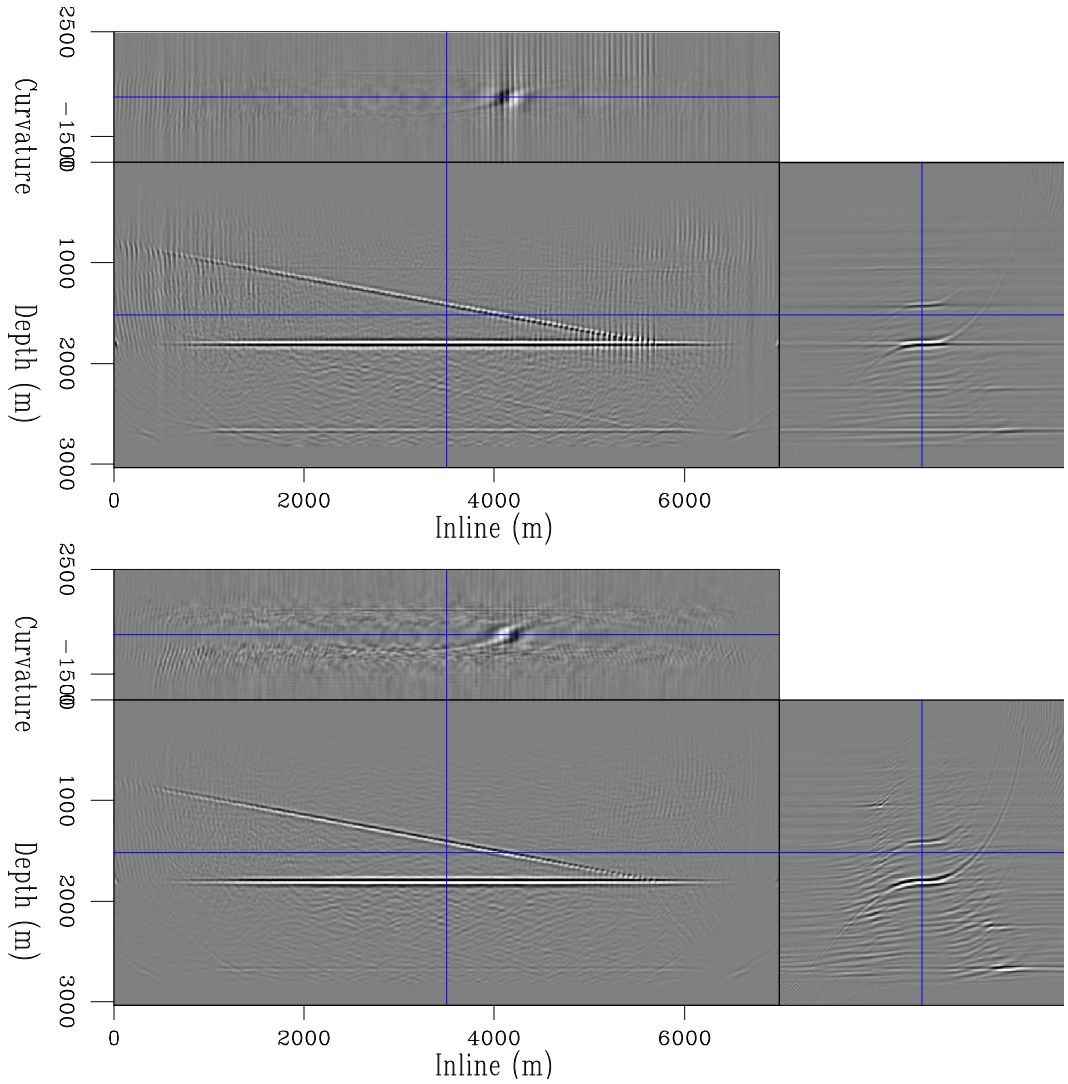

Figure 18: The angle domain image with the correct velocity model after a single parabolic transform (top) and after ten linear iterations of the transform (bottom.) Note the focusing at zero curvature (corresponding to a flat angle gather.) [**CR**]

subsurface reflection events will exhibit a measurable, single-parameter curvature in the angle domain. The other, is that primary events will focus at a similar level of curvature.

The former of these can be quickly disproved by imaging a more complex dataset, with steep structures and discontinuous reflectors. Under these conditions, events in subsurface offset exhibit a far less parabolic nature. Attempts to transform these to the angle domain and isolate primary reflections according to their move-out yielded no success. This is not as severe a limitation for WEMVA, since not every reflector's curvature is needed to be measured in order to back-project a meaningful model update. However, for deblending the loss of reflector information is unnacceptable. Additionally, to build these angle domain panels a regular and dense acquisition geometry is desirable, and this is not a good requirement for a separation engine.

Secondly, the fact that in this example the two events focused at the same measure of curvature was because the velocity model was a scaled version of the true model. If this was not the case, these events would focus to different amounts of curvature. This is not as strict a limitation, since a predetermined range of curvatures could be retained, and significant data-separation still achieved. However, these limitatations coupled imply that curvature-based image-space separation will fail under a variety of conditions.

Instead, posing the separation problem as an inversion will be investigated, where the minimization is posed as a function of these separated data. Initially, how these data behave after demigration will be tested.

Adjoint demigration / Born modeling

As in Chapter 2, for linearized inversion, the adjoint procedure of equation 7 can be used to move back to the data domain. In this case, the forward procedure is now extended Born modeling. For Born modeling, during each imaging time step the receiver wavefield is convolved with the scattering estimate and then propagated. For extended Born modeling, during each imaging time step the receiver wavefield must now be convolved with the extended scattering estimate (this is the extended image.) This is, of course, both more computationally expensive, and requires additional memory. There are additional computation complications involved with extended Born modeling, when compared to extended RTM, and these are discussed at the end of Chapter 6.

To initially illustrate these processes, the same simple two-layer model will be used. This is instructive since all events are readily identifiable. The input, unblended data for these tests is the same as shown in Figure 3, and the correct and incorrect velocity migrations used for forward modeling are the results plotted in Figure 5 and Figure 6.

Applying the adjoint of this extended migration process gives the result in Figure 19, which resembles these input data fairly well. This result is informative of

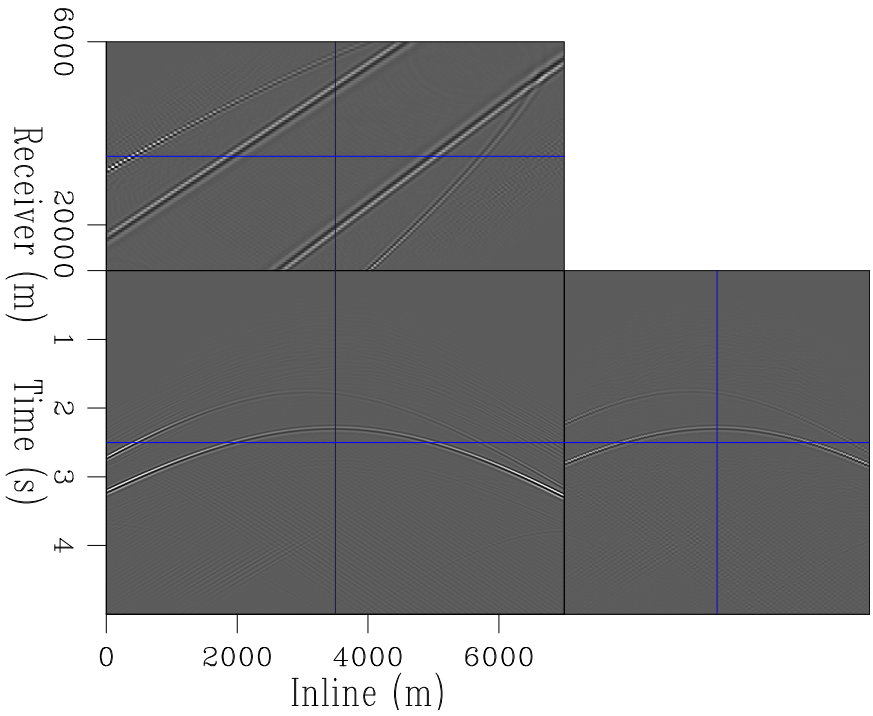

Figure 19: The ouput dataset from one pass of forward modeling, using the correct velocity model. [**CR**]

several attributes of this data recovery process. Amplitudes at early times and short offsets are under-represented; this is indicative of the need to extend the procedure to inversion.

Inverse Born modeling

While extended Born modeling results in the correct kinematic recovery of the input data, the amplitudes are inconsistent. Especially at early times and short offsets; this can be improved upon by extending forward modeling to an inverse procedure. Chapter 2 discussed linearised inversion at length, with the goal of recovering an accurate scattering model. What can be considered as the adjoint and forward procedures can be simply exchanged, and the laws of linear algebra and inversion are all still valid (**?**). Now, what was considered the model (the image) can be considered as the reference data, and what was previously considered the data (the recorded seismic reflections) are contained in what will be considered the model. The inversion scheme will act to recover the dataset that will migrate to provide the (cleaned) input image.

$$J(\mathbf{m}) = \|\mathbf{d} - \mathbf{L}\mathbf{m}\|_2^2 \tag{8}$$

$$J(\mathbf{d}) = \|\mathbf{m} - \mathbf{L}'\mathbf{d}\|_2^2 \tag{9}$$

Equation 8 shows the same objective function which was minimised in Chapter 2, where **L** is the Born modeling operator, **d** is the input data and **m** the scattering model. For inverse Born modeling, the objective function is formulated in equation 9. These will now be expanded into minimization algorithms to explicitly analyse the differences.

Algorithm 1 Extended linearized inversion

Calculate initial data-space residual $r = Em_0 - d$
while iter $<$ n_iter; iter++ **do**
  Create gradient $g_e = E'r$
  Create conjugate gradient $cg = Eg_e$
  Calculate step length
  Update m and data residual
end while
Output model

The algorithm for LSRTM is shown again in algorithm 1. Now, however, L has been replaced with E, to denote the extended imaging operator, and g with g_e, to clarify the increase in dimensionality. The size of the residual and the conjugate gradient are not changed. By switching the sense of the operators, data, model, residual and conjugate gradient, these scheme can be adapted to perform inverse modeling. This is summarized in algorithm 2.

Algorithm 2 Extended inverse Born modeling

Calculate reference extended image $i_e = E'd$
Calculate initial residual $r = E'd_0 - i_e$
while iter $<$ n_iter; iter++ **do**
  Create gradient $g = Er$
  Create conjugate gradient $cg = E'g$
  Calculate step length
  Update d_{out} and image-space residual
end while
Output dataset

? used a similar procedure to remove multiples in the unfocused extended image space, and then used an inverse demigration scheme to recover amplitude consistent, multiple free data. A very similar methodology will be used in this thesis, in the context of data separation.

It is possible to approximate this extended operator, as shown in **?**. This scheme can give an approximate, forward modeled dataset at a substantially lower cost than the full extended operator. However, in a strict inversion formulation it is not an exact adjoint to the imaging procedure. Such an approach could provie a valuable preconditioner to inverse Born modeling, and should be investigated.

Conventional, extended RTM of Figure 3 gave the image seen in Figure 5. In the previous section, a single pass of linearized forward modeling was applied and the output dataset analysed. For inverse Born modeling, this image can be considered the 'data' of the inversion - meaning it is a fixed reference, and is used to calculated the intial residual. Exactly the same procedure as Chapter 2 is run, but with the forward and adjoint operators swapped. The first gradient of the scheme (the adjoint result) is shown in Figure 19. It is immediately clear that the kinematics of the input data have been resolved, but the amplitudes are not correctly balance. As before, the error in the event positioning is incredibly low; the amplitude inconsistencies occur mostly at short offsets and early times.

After running inverse Born modeling for ten iterations the output dataset in Figure 20 is achieved. The amplitude inaccuracies are all fixed, and the error between these data and the input is very low. After only a couple of iterations the normalised residual is below 10%, and after ten iterations this measure is less than 0.03%.

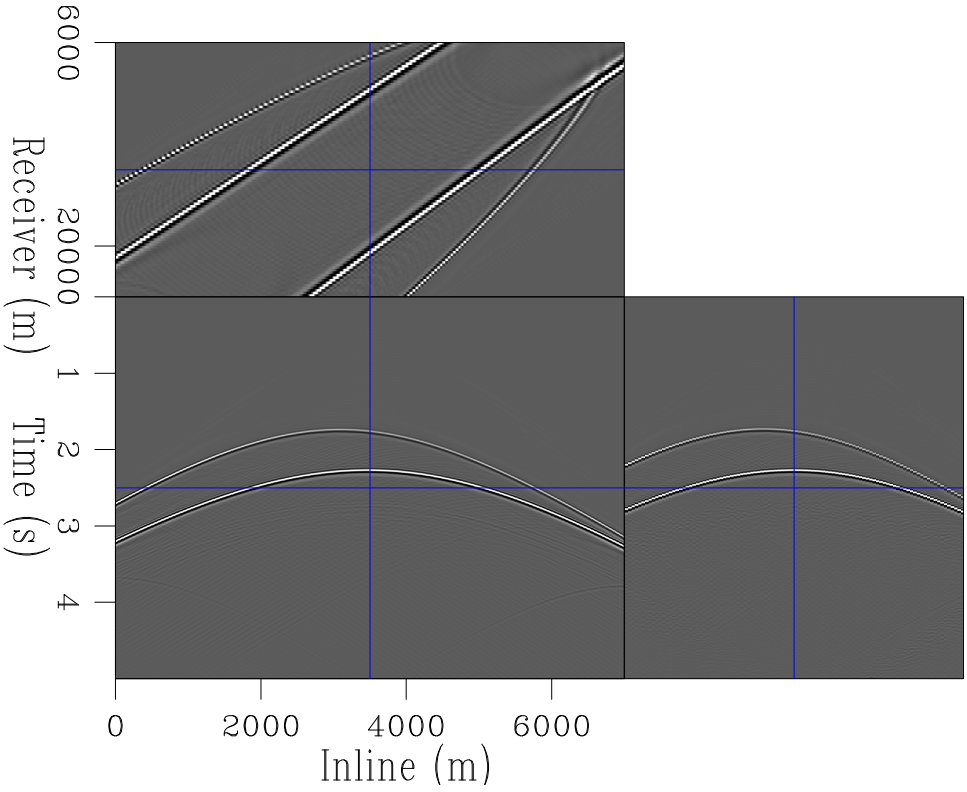

Figure 20: Inverse Born modeling using the correct velocity model, after ten iterations. [**CR**]

To test the algorithm, a very inaccurate velocity model will now be used. The same constant velocity model will be used, which is inaccurate up to 20% in areas.

The first gradient (adjoint) result from incorrect velocity model extended demgration is in Figure 21. Similar to the exact velocity case, the kinematics are (largely) correct, however the amplitudes are not well balanced. This is exacerbated in the

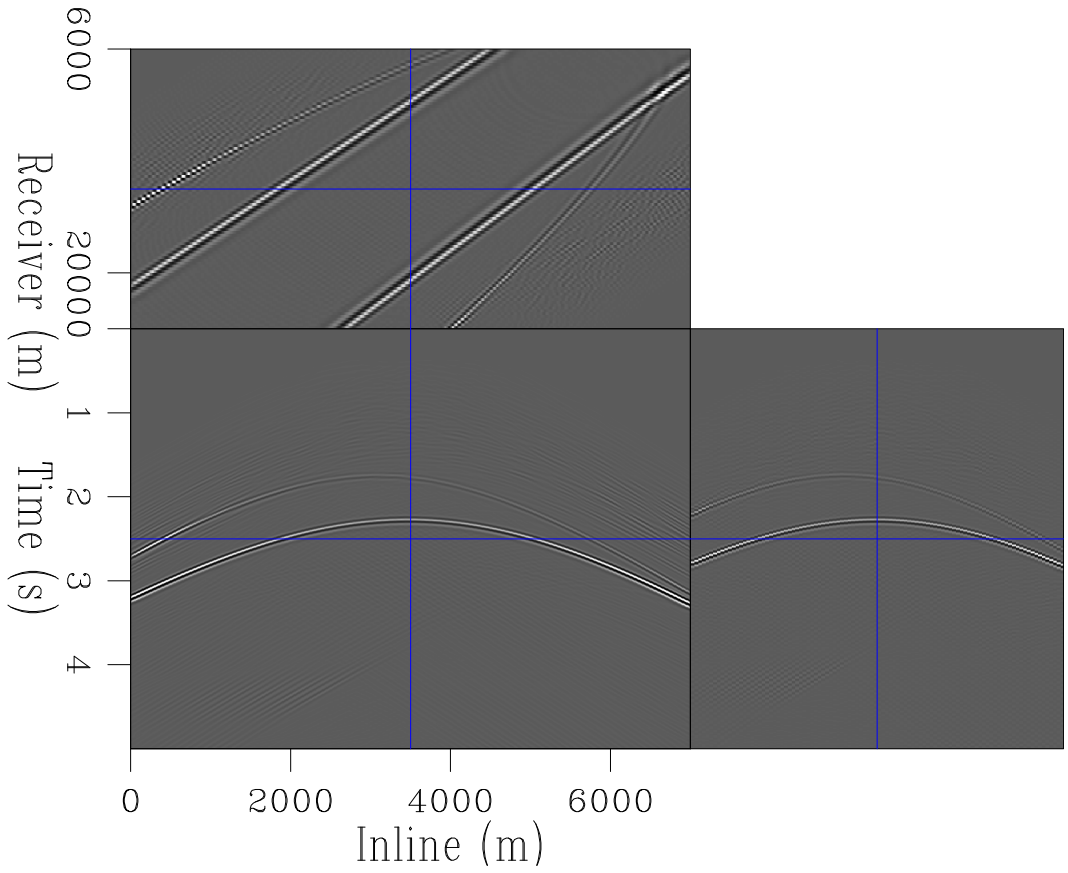

Figure 21: Adjoint Born modeling using an incorrect velocity model, after ten iterations. [**CR**]

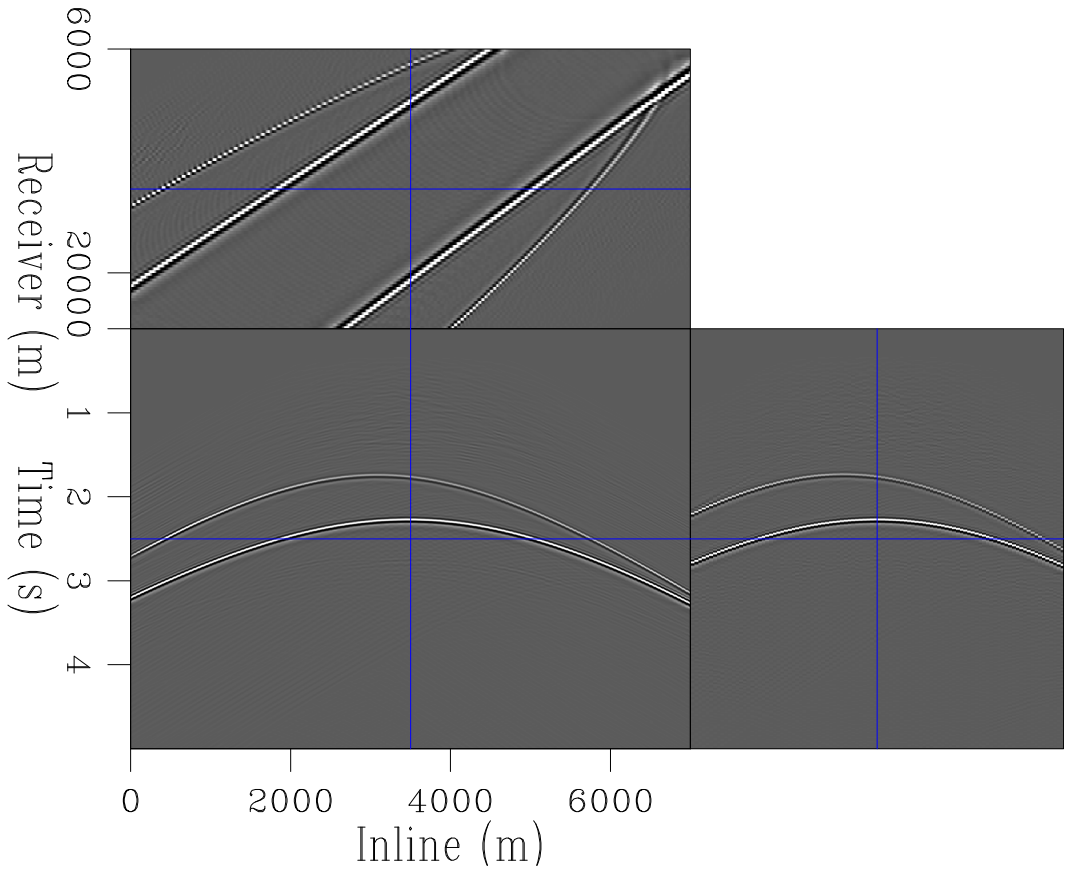

Figure 22: Adjoint Born modeling using an incorrect velocity model, after ten iterations. [**CR**]

rough model case, and in addition to these amplitude inconsistencies, there are more artifacts induced. These arise, from the extended Born modeling. The recovered data after ten iterations are plotted in Figure 22. As before, the inversion has acted to correctly balance these amplitudes and the output dataset closely resembles to input data, to within 0.3% error.

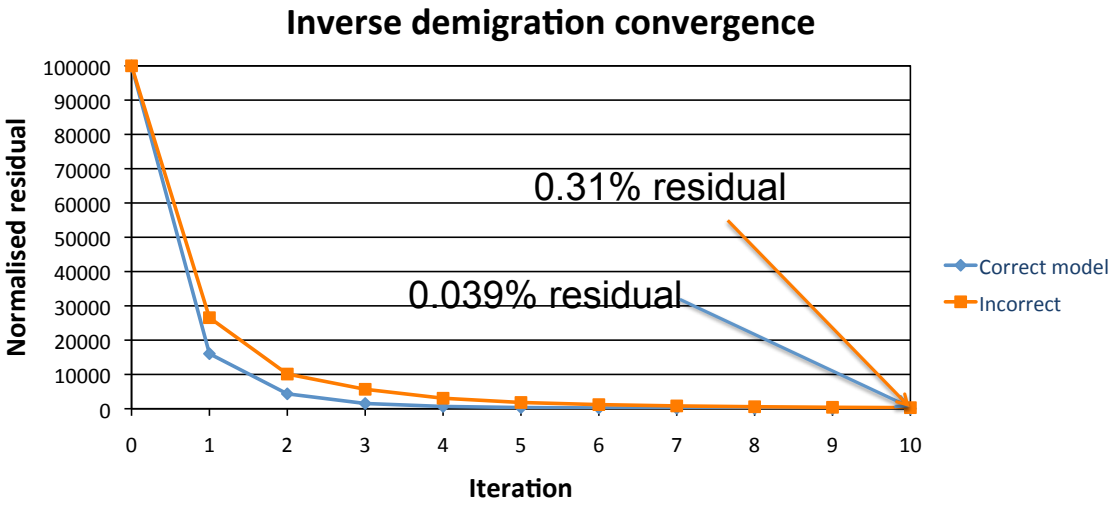

Figure 23: Convergence of inverse Born modeling as a function of iteration number. The normalised residual is measured in the image space. [**NR**]

The convergence curve for both schemes are plotted in Figure 23. Unsurprisingly, the extended scheme is slower to converge than the exact model scheme. Again, within one iteration a residual of less than 10% is achieved, and after ten iterations these output data are correct to within 0.3%. This is a very acceptable level of error, particularly for a scheme which will be augmented with velocity updates.

These results demonstrate that extended inverse Born modeling can successfully recover input data, even after imaging with an incorrect velocity model. A similar approach can now be used, with the goal of data separation, rather than simple amplitude recovery.

IMAGE SPACE DEBLENDING

While primary blending is fixed post-acquisition, the style of proposed processing can influence how these data are initially acquired. Intuitively, the factors that will influence these blended data are: the number of sources, the minimum recharge time for the airguns, the randomness of shot positionings, the randomness of shot timings, receiver geometry, and to a lesser extent, the number of receivers and the proposed recording length.

As mentioned earlier in this chapter, existing separation methods are critically

dependent on the randomness of the source timings. Any induced repetition or predictability in these can induce debilitating artifacts (**?**). In the case of constant delays between shots, these methods entirely fail. For both flexibility, and confidence, in acquiring simultaneous data, it is desirable to relinquish these restrictions. The aforementioned three styles of shooting will be analysed in these upcoming sections: random delays, linear delays, and pseudo-linear delays.

Marmousi data separation

Figure 10, Figure 12 and Figure 14 show the extended images produced from these three datasets using the correct velocity. The differences in blending are manifested in the image space, although the coherency differences are not as pronounced as intuition may suggest. Even the linearly blended data becomes well dispersed in the image space. The artifacts are more coherent, but the focusing characteristics of the primary events, and the differences in contrast, suggest that separation should be possible.

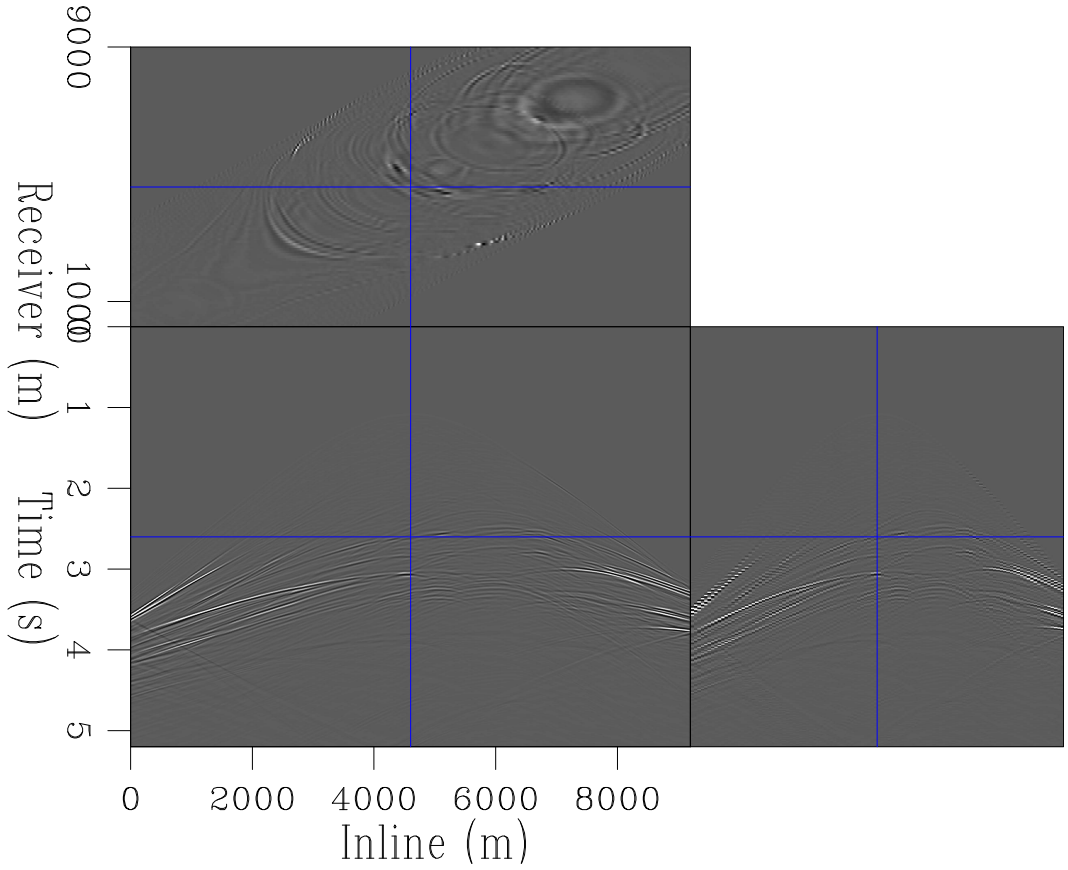

Figure 24: The output dataset after applying one pass of Born modeling to Figure 10, which was the image created from a randomly delayed dataset. [**CR**]

The recovered datasets after adjoint separation can be seen in Figure 24, Figure 25

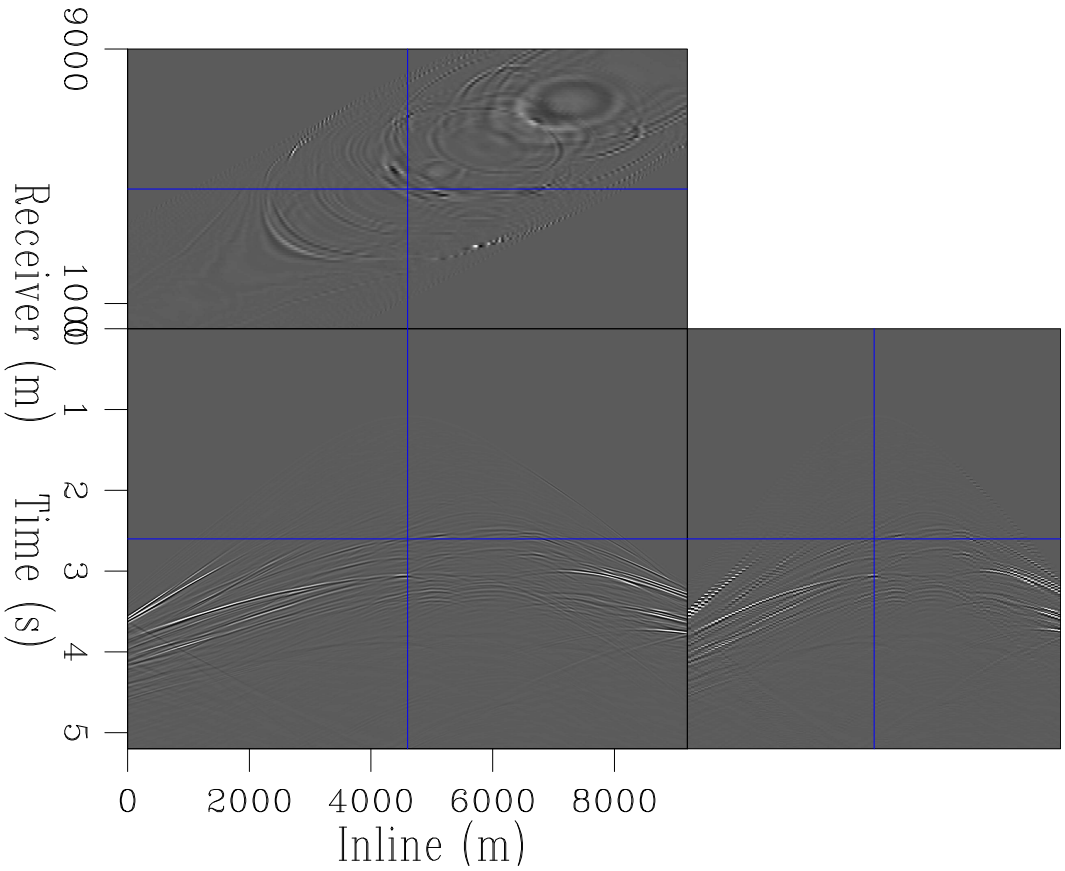

Figure 25: The output dataset after applying one pass of Born modeling to Figure 12, which was the image created from a linearly delayed dataset. [**CR**]

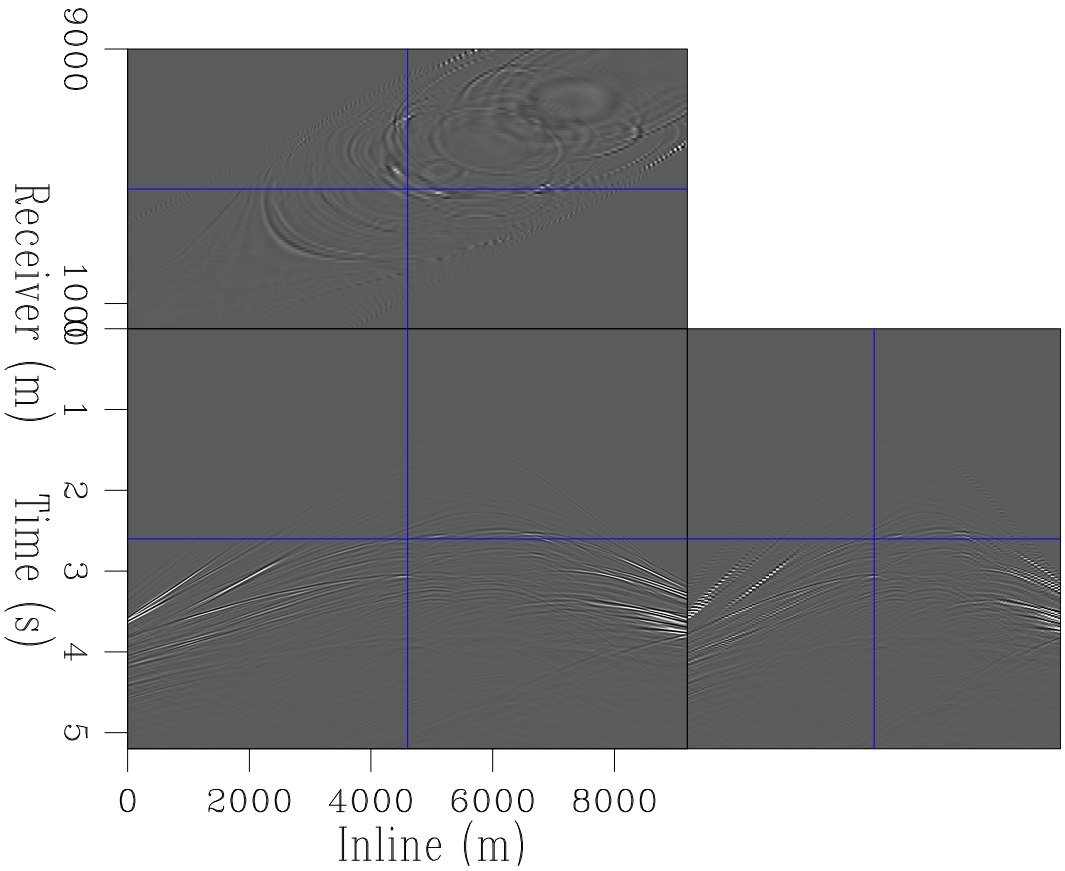

Figure 26: The output dataset after applying one pass of Born modeling to Figure 14, which was the image created from a pseudo-linearly delayed dataset. [**CR**]

and Figure 26. These can be contrasted with the reference, unblended dataset, in Figure 8. Each of the blending schemes have been well separated and the resultant datasets could be used for conventional velocity estimation and imaging. Again, amplitudes at early times and shot offsets are weaker than in Figure 8, which should be the result if the separation was exact. This can be improved upon by using the inverse scheme.

It should be noted that there are some fractionally more coherent artifacts in the recovered data from the linear encoding. Nonetheless this methodology separated these linearly delayed data very accurately.

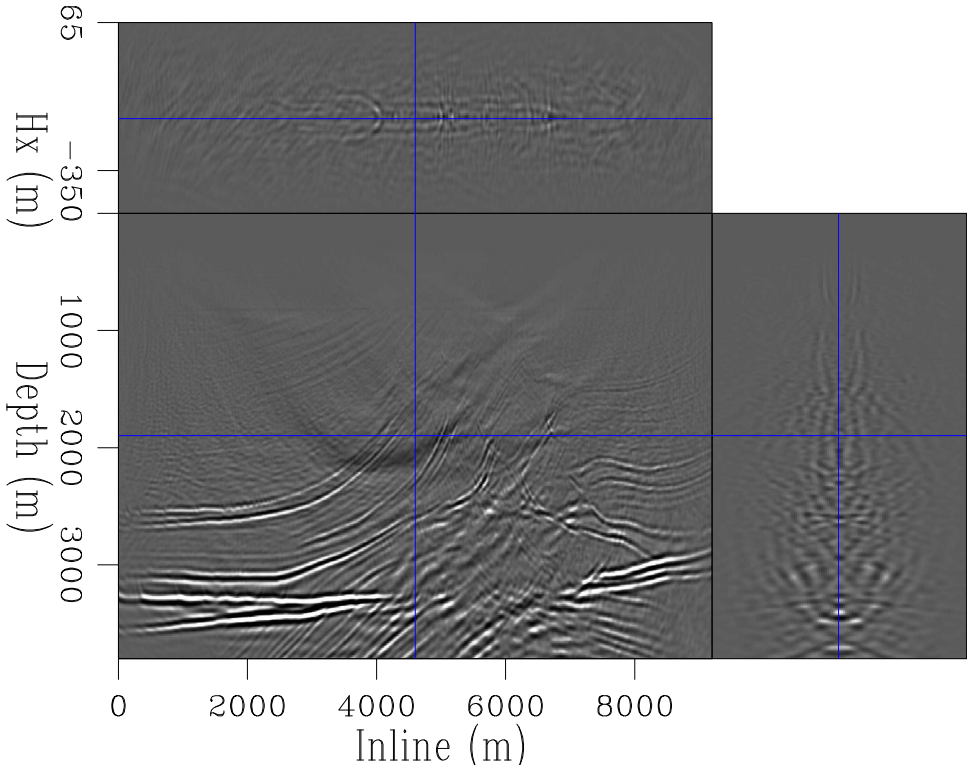

Figure 27: The extended image from migrating Figure 13 (data with constant delays) using a rough velocity model. [**CR**]

Figure 27 shows the result from migrating these data, but using an inaccurate velocity model. The primary events are now not well focused at zero-subsurface offset, and the focusing contrasts between primary and secondary events is far less. Energy of interest now spans many of the acquired subsurface offsets and distinguishing events from primary and secondary energy is less obvious. Separation as an inverse problem was not run on these data, a more complicated model was used instead.

Using data acquired over the Marmousi model gives informative results about the suggested procedure, but to further confidence over this methodology a more difficult example must be used. A section of the SEAM model was windowed, featuring rugose reflectors, continuous reflectors and a steep salt body with carbonate top

and sedimentary inclusions. These attributes comprise many of the difficulties of contemporary imaging targets. If this separation method can perform well over these data then much stronger conclusions can be made.

Blended inversion

Adapting linearised inversion to inverse forward modeling involved reversing the operators, and the sense of what was the model and what was the data. Creating a blended inversion scheme to recover separated data involves an extra step, since the blending must be accounted for.

$$\mathbf{d}_b = \mathbf{\Gamma} \mathbf{d}_s \tag{10}$$

If $\mathbf{d}_s$ denoted the separated data, $\mathbf{d}_b$ the blended data, and $\mathbf{\Gamma}$ the operator that creates these blended data (applies the time shifts), then the blending can be described as equation 10. This operator, $\mathbf{\Gamma}$, contains all the necessary time shifts to move between the domains, and takes an continuous, input dataset. It windows this input dataset according the source times and a desired recorded length, and outputs a series of shot gathers. Of course, these shot gathers will contain blended contamination, since individual shots have simply been windowed and no separation has been attempted. This process of windowing and aligning is sometimes referred to as pseudo-deblending.

$$\mathbf{m} = \mathbf{L}'\mathbf{\Gamma}'\mathbf{d}_b \tag{11}$$
$$\mathbf{m}_e = \mathbf{E}'\mathbf{\Gamma}'\mathbf{d}_b \tag{12}$$

As earlier, $\mathbf{L}'$ can represent the zero-offset imaging operator, and $\mathbf{E}'$ the extended imaging operator. The input, blended data can be cut and aligned, using $\mathbf{\Gamma}$, and then migrated, using either operator. This results in either a zero-offset image or an extended image, shown in equation 11 and equation 12 respectively. These images can then be used for forward modeling, or for inverse Born modeling. Cost functions, similar to those in Chapter 2, can then be minimized. Now, the function will aim to reduce the misfit related to $\mathbf{d}_s$, the separated dataset.

$$J(\mathbf{d}_s) = \|\mathbf{L}'\mathbf{d}_s - \mathbf{m}\|_2^2 \tag{13}$$
$$J(\mathbf{d}_s) = \|\mathbf{E}'\mathbf{d}_s - \mathbf{m}_e\|_2^2 \tag{14}$$

A similar algorithm to algorithm 2 is then used; the new zero-offset and extended objective functions to be solved are formulated in equation 13 and equation 14, and this adapting algorithm expanded as algorithm 3. These new objective functions are

extensions of equation 9, with $\mathbf{\Gamma}$ included. By making this extended image the input for an inverse Born modeling scheme, these data can be effectively separated into individual shot records.

Algorithm 3 Inverse deblending

Calculate reference extended image $i_e = E'\Gamma' d$
Calculate initial residual $r = E'd_0 - i_e$
while iter < n_iter; iter++ **do**
  Create gradient $g = Er$
  Create conjugate gradient $cg = E'g$
  Calculate step length
  Update d_{out} and image-space residual
end while
Output dataset

To demonstrate the effectiveness of minimising equation 14 for shot separation, a model and dataset more complex than Marmousi will be used. A same section of the SEAM model that was used in Chapters 2 and 3 was used, since this features steep deeps, high velocities, and a range of scattering contrasts. While the Marmousi tests were informative, it does not feature these final two attributes.

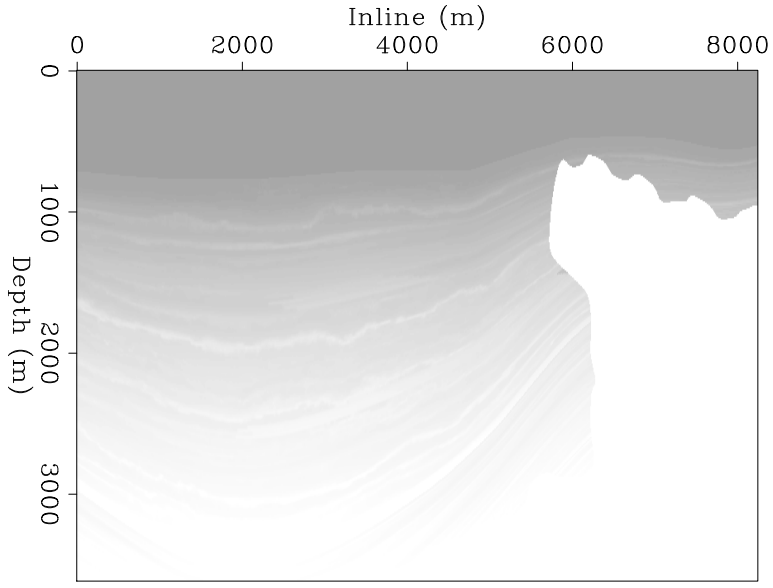

Figure 28: The velocity model windowed from the SEAM model, used for a more realistic separation test. [**ER**]

As a reminder, the velocity model used for simulating the comparison, unblended data is shown in Figure 28, and the reference dataset can be seen in Figure 29. A pseudo-linear blending scheme was implemented, since this is the most realistic and can pose separation problems. These data after blending are plotted in Figure 31.

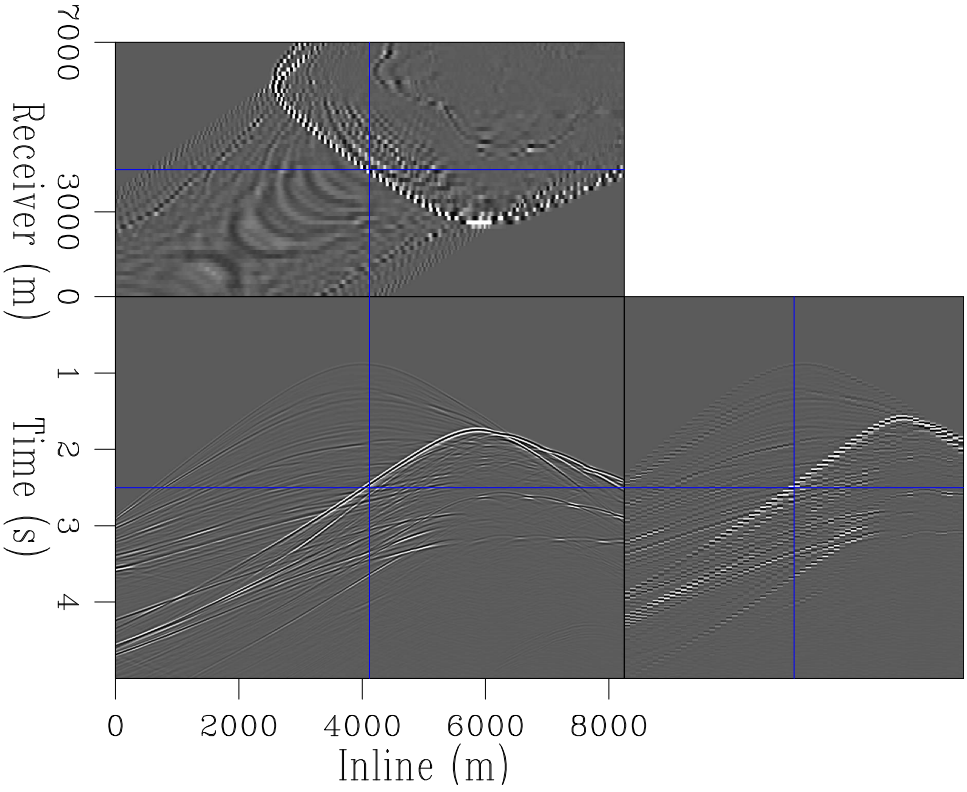

Figure 29: A conventional dataset acquired using the section of the SEAM model. [**CR**]

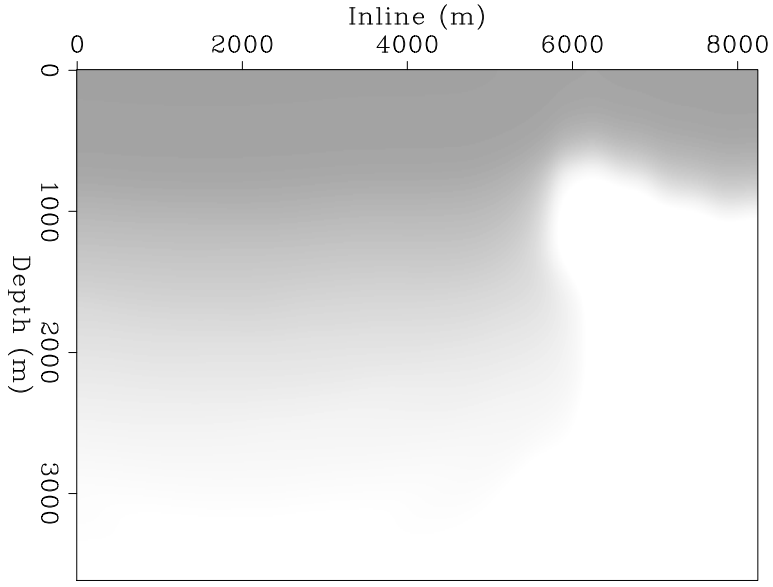

Figure 30: A heavily smoothed version of Figure 28, used for inaccurate model separation. A rectangle filter of 30 model points x 30 model points was used. [**ER**]

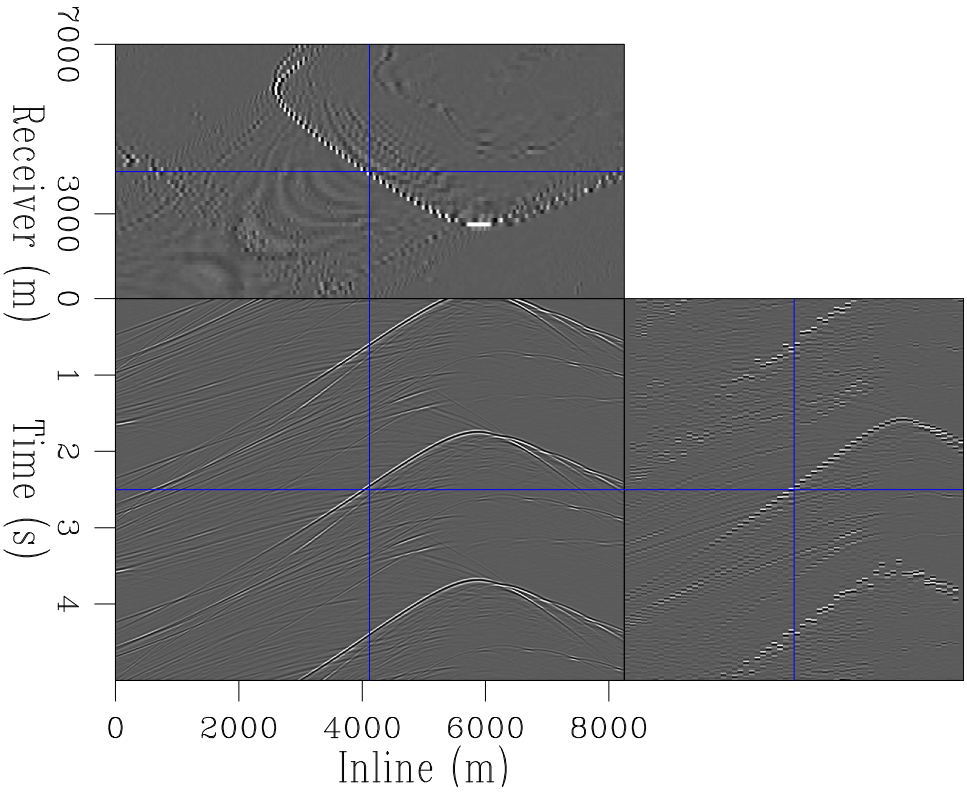

Figure 31: A pseudo-linearly blended dataset acquired using the section of the SEAM model. [**CR**]

An approximate, unfocused image was created in the extended image space by massively smoothing the input velocity model, creating some regions where the velocity is approximately, and some regions where the velocity incorrect up to 15%. This is more realistic than simply scaling the full model, and will create a very loosely focused salt boundary, creating a valid separation test. The inaccurate model used is plotted in Figure 30, and the loosely focused, noisy image after migration, in Figure 32. After ten iterations of this inverse deblending process (algorithm 3), the output, separated dataset is shown in Figure 34. Through comparison to the input, blended dataset, this scheme has been very successful in separating these shots into uncontaminated gathers. No remaining energy from the interfering data remain in these separated shots, however a few, minor artifacts from extended modeling remain.

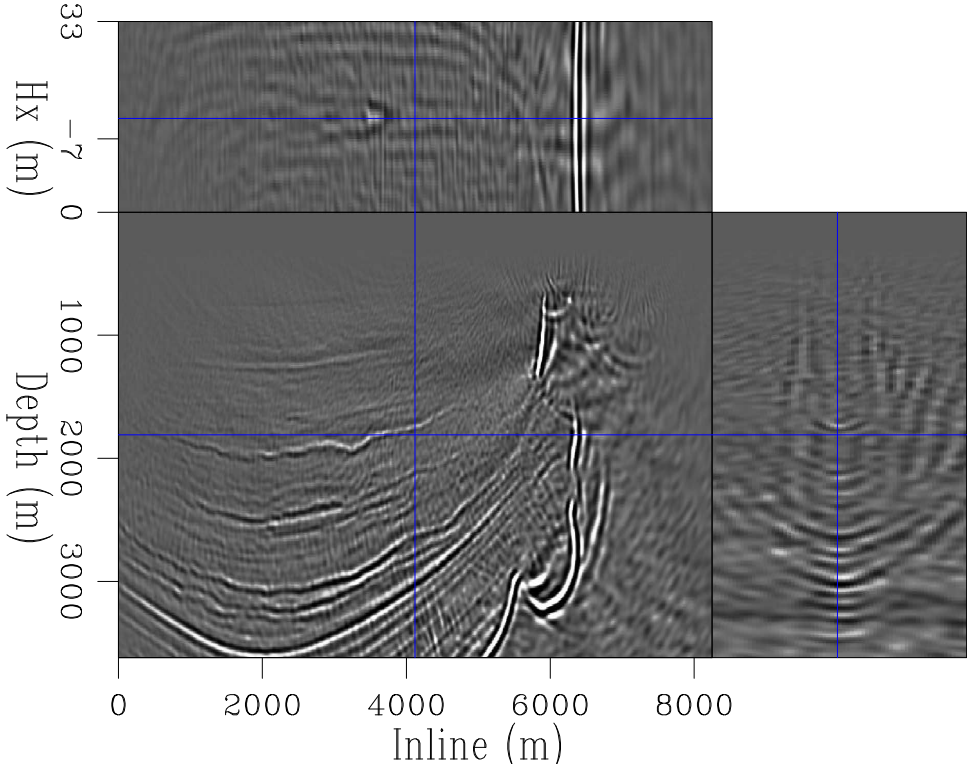

Figure 32: The extended image created by migrating the blended dataset with the velocity model shown in Figure 30. [**CR**]

Figure 35 shows the results of applying RTM to Figure 29, Figure 33 and Figure 34 respectively. It is clear that all images are directly comparable, although a small amount of noise is noticeable within the salt body in the two lower images. The salt boundary is slightly less smooth in the image using the data separated with the inaccurate model, however this is the only obvious imperfection. Using the heavily smoothed model does not appear to have resulted in the loss of any information.

Extended images produced by migrating 30 shots before and after deblending are shown in Figure 36 and Figure 37, using the rough migrating velocity. Due to the inaccurate model, both images are unfocused and noisy, but the image after deblending

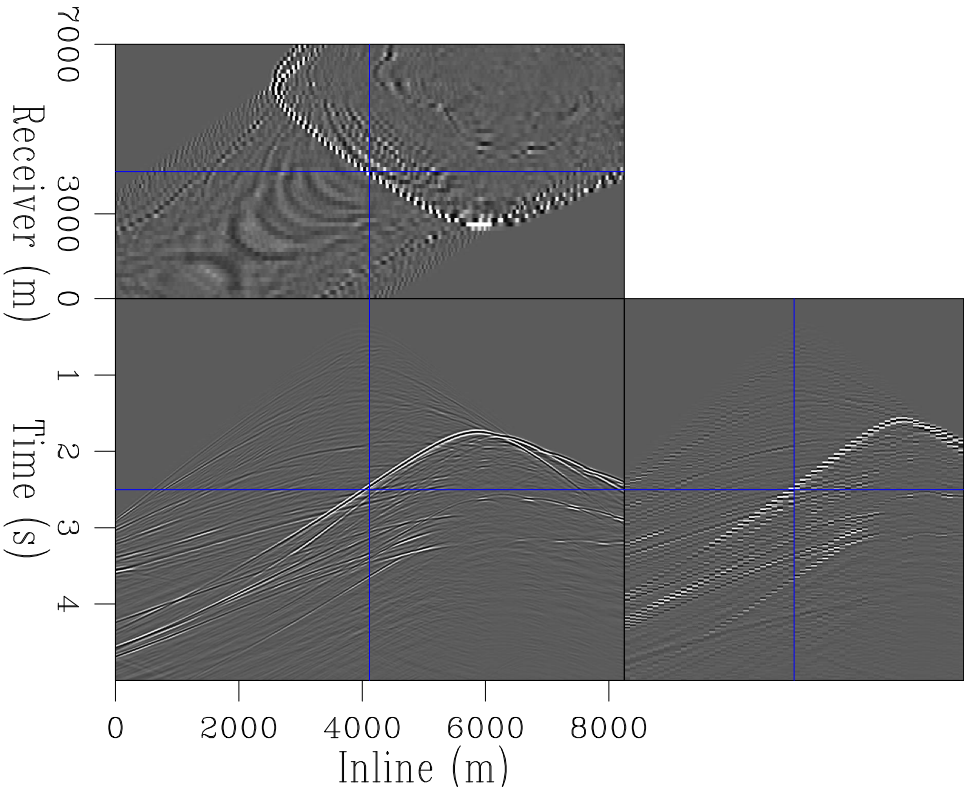

Figure 33: The output separated data after 10 iterations of inverse deimgration using the correct velocity model. [**CR**]

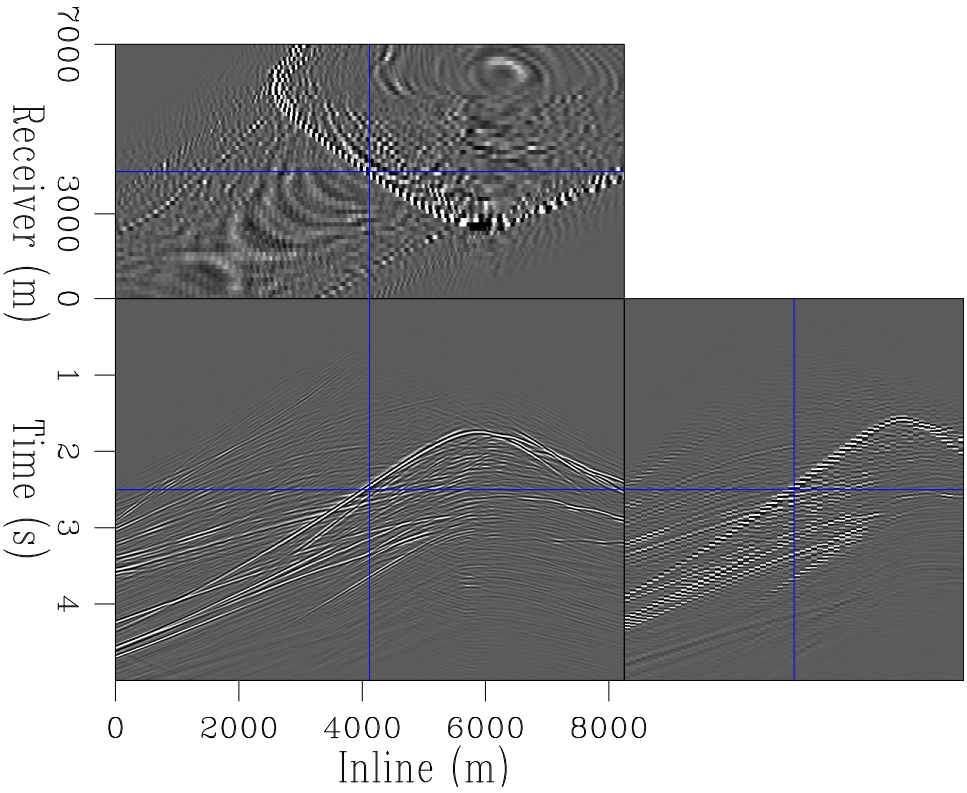

Figure 34: The output separated data after 10 iterations of inverse deimgration using an inaccurate velocity model. [**CR**]

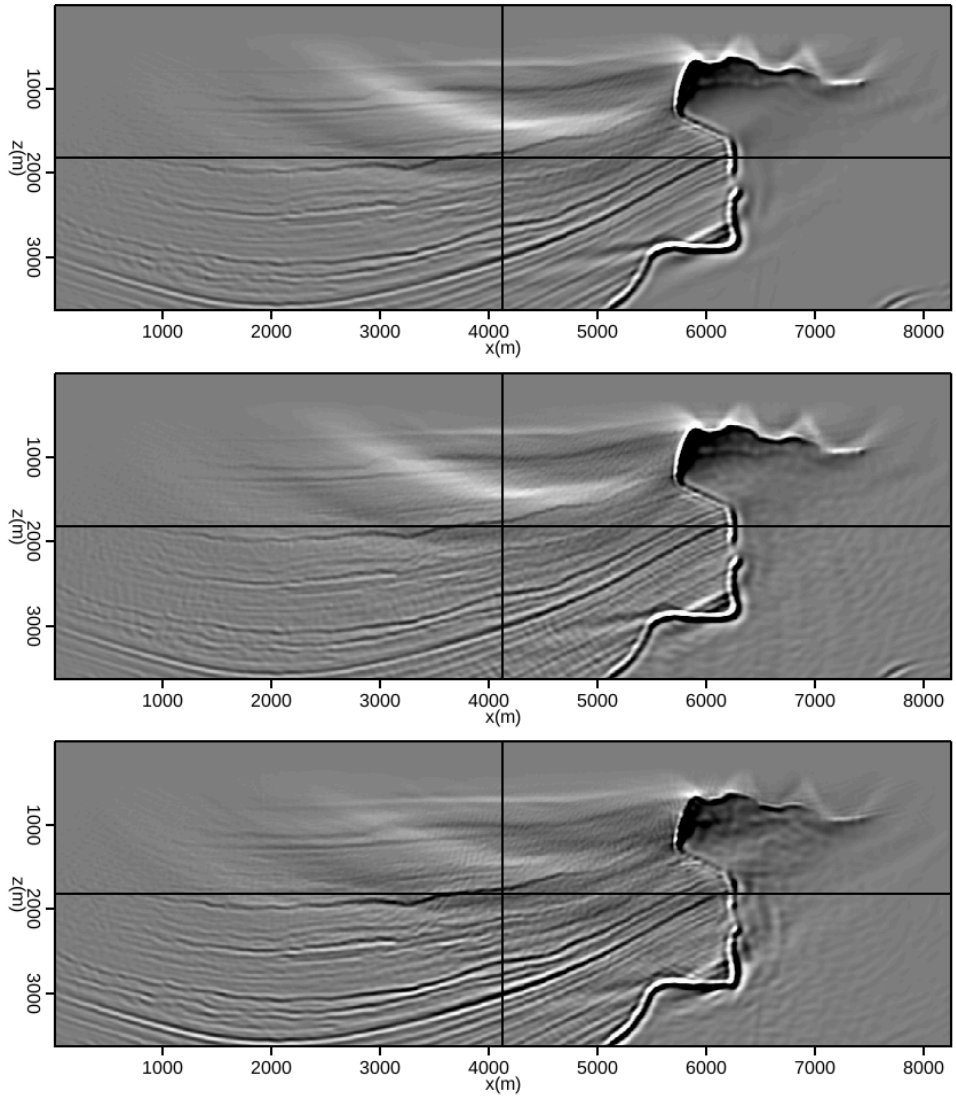

Figure 35: Images created from conventionally acquired data, blended data separated using the correct velocity, and blended data separated using an inaccurate velocity model respectively.

is substantially cleaner, and would be easier to perform preliminary interpretations on, as well as moveout based estimations. Often for quick velocity updates / QC checks a subset of the data will be used, and this demonstrates the effectiveness of performing separation first.

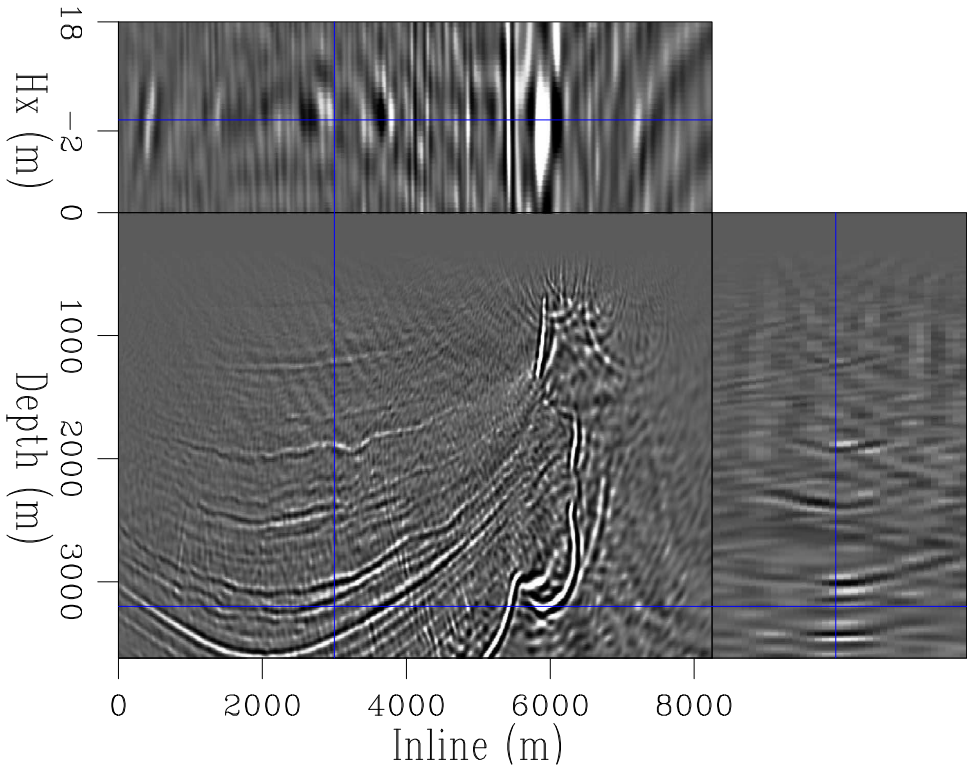

Figure 36: Thirty shots migrated into the extended domain before deblending, using the inaccuarte separation velocity. [**CR**]

The convergence to the input dataset is shown in Figure 38. This was calculated by reblending the output data, and comparing to the input blended data. Since the only input is the blended data, $\mathbf{d}_b$, then to measure separation these output data, $\mathbf{d}_s$, should be reblended, and the output compared to $\mathbf{d}_b$. Other quantitative measures could be misleading, so $\|\mathbf{d}_b - \mathbf{\Gamma} \mathbf{d}_s\|_2^2$ is plotted. The system deblends the data almost immediately, and requires iterations to recover the amplitude content of the input data, and to reduce modeling artifacts. This process does not converge to as low a residual as unblended inverse linearized forward modeling (Figure 23), but considering how much more complex the model and data were for this SEAM test, it does a very comparable job.

CONCLUSIONS

Primary blending poses many more processing and imaging challenges than secondary blending, due to the fact the the blending is fixed. For field blended data to integrate

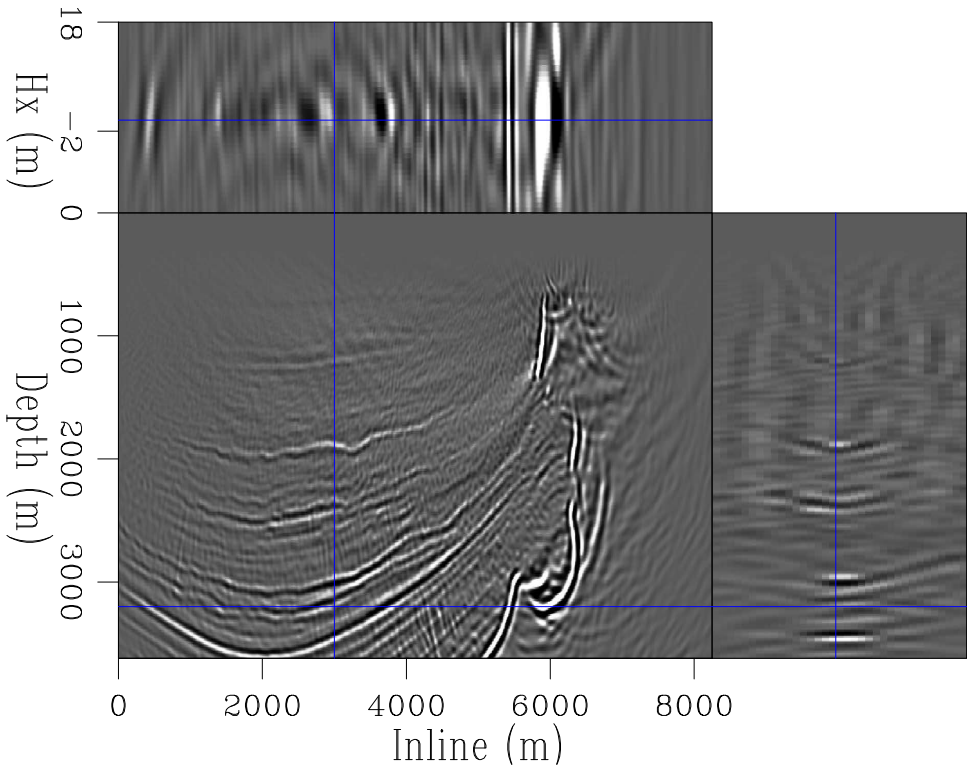

Figure 37: Thirty shots migrated into the extended domain after deblending, using the inaccurate separation velocity. [**CR**]

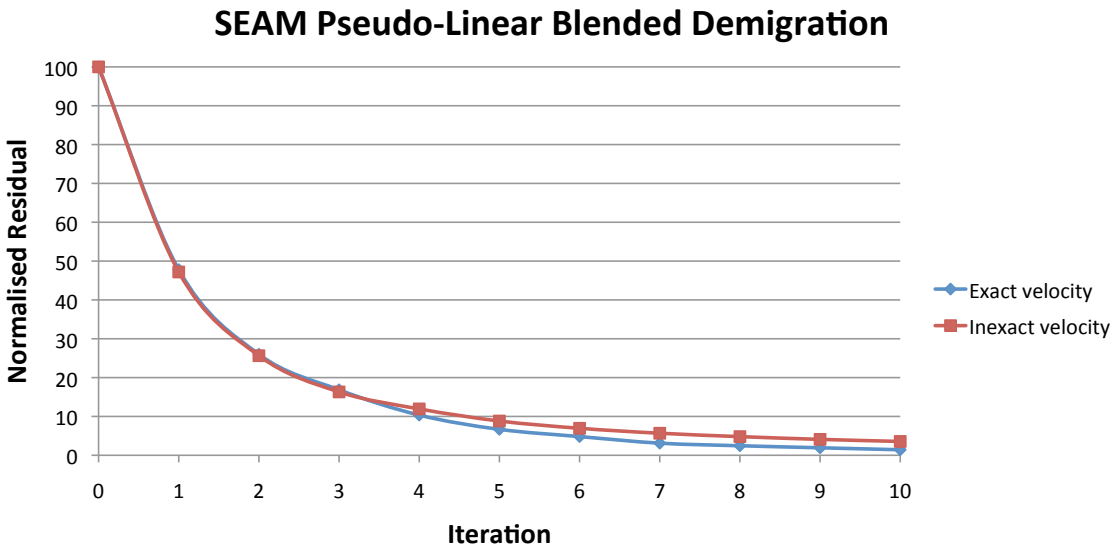

Figure 38: How the separation algorithm performs, for SEAM, as a function of iteration number. This normalised residual is the L2 norm of the difference between the input, blended data, and the output, separated data after reblending. [**NR**]

well into existing processing and imaging work flows, the ability to separate these data into their conventionally acquired equivalent dataset is desirable.

The image space provides a powerful transform for this separation, since even with constantly delayed data many high amplitude blending-related artifacts are stacked out, and for randomly blended data the separation is provided almost immediately. By formulating the imaging in the extended image space a good velocity model requirement can be relaxed, since all kinematic and amplitude information for the primary data is saved, and the overlapping data is still massively reduced in both focusing and moveout characteristics.

For simple, layered models it is possible to isolate these overlapping data as a function of their curvature, however for more complex data this is not possible. Instead, by fixing this extended image and posing data recovery as an inverse, extended Born modeling problem, a separated dataset with comparable amplitudes and correct kinematics can be constructed.